THE METALLICITY EVOLUTION OF INTERACTING GALAXIES

Paul Torrey[1], T. J. Cox[2], Lisa Kewley[3], and Lars Hernquist[1]
[1] Harvard Smithsonian Center for Astrophysics, 60 Garden St., Cambridge MA 02138
[2] Observatories of the Carnegie Institute of Washington, 813 Santa Barbara St., Pasadena CA 91101
[3] Research School of Astronomy & Astrophysics, Mount Stromlo Observatory, Cotter Road, Weston Creek, ACT 2611, Australia

ABSTRACT

Nuclear inflows of metal-poor interstellar gas triggered by galaxy interactions can account for the systematically lower central oxygen abundances observed in local interacting galaxies. Here, we investigate the metallicity evolution of a large set of simulations of colliding galaxies. Our models include cooling, star formation, feedback, and a new stochastic method for tracking the mass recycled back to the interstellar medium from stellar winds and supernovae. We study the influence of merger-induced inflows, enrichment, gas consumption, and galactic winds in determining the nuclear metallicity. The central metallicity is primarily a competition between the inflow of low-metallicity gas and enrichment from star formation. An average depression in the nuclear metallicity of ∼0.07 is found for gas-poor disk–disk interactions. Gas-rich disk–disk interactions, on the other hand, typically have an enhancement in the central metallicity that is positively correlated with the gas content. The simulations fare reasonably well when compared to the observed mass–metallicity and separation–metallicity relationships, but further study is warranted.

Key words: galaxies: abundances – galaxies: evolution – galaxies: interactions – galaxies: ISM

Online-only material: color figures

1. INTRODUCTION

The nuclear metallicities of star-forming galaxies are characterized by a mass–metallicity (hereafter MZ; Lequeux et al. 1979; Rubin et al. 1984; Tremonti et al. 2004) relation. Contributing to the scatter in the MZ relation are interacting galaxies, which are consistently lower in central metallicity than non-interacting systems of equivalent mass, as first noted by Kewley et al. (2006), and later confirmed for ultra-luminous infrared galaxies (Rupke et al. 2008), close pairs in the Sloan Digital Sky Survey (SDSS; Ellison et al. 2008; Michel-Dansac et al. 2008; Peeples et al. 2009; Sol Alonso et al. 2010), and local, low-mass systems (Ekta & Chengalur 2010). Observations such as these are most naturally explained as the result of vigorous merger-induced inflows of gas (Barnes & Hernquist 1991, 1996) which rearrange the initial metallicity gradient (Shields 1990; Belley & Roy 1992; Zaritsky et al. 1994; MacArthur et al. 2004) and "dilute" the nuclear metallicity (Kewley et al. 2006). In this sense, the same gas that drives nuclear starbursts (Mihos & Hernquist 1994b, 1996; Iono et al. 2004) and triggers central active galactic nucleus (AGN) activity and black hole growth (Di Matteo et al. 2005; Springel et al. 2005; Hopkins & Hernquist 2006; Hopkins et al. 2007), also results in suppressed nuclear metallicity.

Simulations of merger-driven inflows of gas naturally predict a flattening of the initial metallicity gradient (Perez et al. 2006; Rupke et al. 2010a; Perez et al. 2011), which has now been observed in a number of colliding systems (Kewley et al. 2010; Rupke et al. 2010b). However, more than hydrodynamics are at play in determining the nuclear metallicity evolution. To further our understanding, we should consider ongoing star formation with associated chemical enrichment, feedback from star formation and AGN activity, and the interchange of material between the stellar and gaseous phases as stars are born and later return material to the interstellar medium (ISM).

The four main processes responsible for the evolution of the nuclear metallicity are gas inflows, chemical enrichment from star formation, gas consumption, and galactic outflows. These effects compete with one another to influence the nuclear metallicity, making it difficult to determine their relative importance a priori. Numerical simulations have only recently been used to quantify the detailed impact of these effects on metallicity gradients and nuclear metallicities of interacting pairs. Rupke et al. (2010a) simulated colliding galaxies without chemical enrichment to explore dynamically induced changes in metallicity gradients, finding that a drastic flattening can occur, accompanied by a drop in the nuclear metallicity. Montuori et al. (2010) and Perez et al. (2011) performed simulations with star formation and chemical enrichment and found similar results to Rupke et al. (2010a), but noted that the dip in the nuclear metallicity values can be counteracted by chemical enrichment from star formation. These simulations have refined our knowledge of the depressed MZ relation.

In this paper, we explore the evolution of the nuclear metallicity during mergers using numerical simulations which include cooling, star formation, stellar feedback, and black hole growth and AGN feedback. Our approach allows us to systematically investigate the importance of gas inflows, chemical enrichment from star formation, gas consumption as a result of star formation, and galactic outflows. In order to unambiguously determine the role of metal enrichment, we have developed a stochastic method to recycle stellar particles back to the ISM without requiring inter-particle mass mixing. The stochastic gas recycling method, which is designed by analogy to the widely used stochastic star formation method, has attributes that are distinct from kernel-weighted mass return, making it particularly useful for our study.

We consider a range of situations with systematically varied parameters to enhance our understanding of metallicity evolution as a natural extension of the merger process. We find that, for systems modeled after those in the local universe, the main driver behind changes to the nuclear metallicity is the flow of low-metallicity gas to the nuclear regions or metallicity dilution. However, we identify two previously underappreci-

ated effects that influence the strength of this dilution: locking of gas and metals in the stellar phase, and gas and metal removal via stellar-driven winds. We also find that, for systems modeled after high-redshift galaxies, the main driver of the nuclear metallicity shifts to chemical enrichment. In these simulations, the nuclear metallicity increases, contrary to what is observed in the local universe, suggesting that the interacting galaxy MZ relation may evolve differently at high redshifts.

We compare our simulations directly to observations by synthesizing a population of progenitor galaxies with properties consistent with observed samples and show that the empirical depression in the close-pair MZ relation can be reproduced while accounting for chemical enrichment. We find good agreement between our simulations and observations for both the interacting galaxy MZ relation and separation–metallicity (SZ) relation.

2. METHODS

We employ a library of merger simulations carried out using the N-body/smooth particle hydrodynamics (SPH) code GADGET-2 (Springel 2005). GADGET-2 is based on a formulation of SPH (Springel & Hernquist 2002) which conserves both energy and entropy simultaneously (when appropriate). In addition to accounting for gravity and hydrodynamics, our simulations also include a sub-grid two-phase model of star formation, supernova feedback, radiative cooling of gas, and star-formation-driven winds (Katz et al. 1996; Springel & Hernquist 2003, hereafter SH03). These features give a working description of the multiphase nature of the ISM (e.g., McKee & Ostriker 1977) without explicitly resolving the various phases. Supermassive black hole sink particles are included in our simulations and have both accretion and thermal feedback associated with them, but their presence does not influence any results presented in this paper.

The simulations presented here also include a novel method for returning gas to the ISM from (prompt) supernovae and asymptotic giant branch (AGB) winds. While the main body of our simulations code has been used for numerous other studies (see, e.g., Cox et al. 2006a, 2006b; Robertson et al. 2006a, 2006b, 2006c), the inclusion of time-delayed gas recycling is a new feature which is described.

2.1. The Basic Model: SH03

The primary astrophysical processes modeled in our simulations—including cooling, star formation, feedback, and galactic winds—are included as in the SH03 model. Because these processes are discussed extensively in that paper we review them only briefly here.

The instantaneous rate of star formation for an SPH particle is given by

$$\frac{dM_*}{dt} = \frac{M_c}{t_*},\qquad(1)$$

where M_* is the stellar mass, M_c is the mass of cold gas (i.e., some fraction of the SPH particle's mass that is in the cold phase as determined via the sub-grid model prescription of SH03), and t_* is a characteristic star formation timescale. We adopt a value $t_* = 4.5$ Gyr so that our simulations are consistent with the Kennicutt–Schmidt relation (Schmidt 1959; Kennicutt 1998; Cox et al. 2006b). Star formation is assumed to only take place in gas which has densities above a set threshold, which in our case is 0.5 cm^{-3}.

Equation (1) is used as the basis for a Monte Carlo method for actually converting SPH particles to star particles. Each SPH particle is assigned a probability of turning into a star particle as follows:

$$p_* = \left[1 - \exp\left(-\frac{\Delta t}{t_{\mathrm{SFR}}}\right)\right],\qquad(2)$$

where Δt is the current simulation time step and $t_{\mathrm{SFR}} = M_{\mathrm{gas}}/(dM_*/dt)$ is the star formation timescale. A particle is converted if a random number drawn between 0 and 1 is less than Equation (2).

The instantaneous rate of mass launched in star-formation-driven winds is given by

$$\frac{dM_w}{dt} = \gamma \frac{dM_*}{dt},\qquad(3)$$

where dM_*/dt is the local star formation rate and γ is the mass entrainment efficiency. We typically take $\gamma = 0.3$, which is the mean value for luminous infrared galaxies measured by Rupke et al. (2005), and the resulting winds are ejected at $v_w = 242$ km s^{-1}.

Equation (3) is used as the basis for a Monte Carlo method for wind generation. The associated probability of launching a particle in a wind is given by

$$p_w = \left[1 - \exp\left(-\frac{\Delta t}{t_w}\right)\right],\qquad(4)$$

where $t_w = M_{\mathrm{gas}}/(dM_w/dt)$. Particles put into winds receive a velocity kick and are not allowed to interact with the surrounding medium while they leave their host environment. In principle, gas particles launched by winds may still contribute to the nuclear gas-phase metallicity. However, in practice, these particles very quickly leave the nuclear regions and no longer contribute to the nuclear metallicity.

2.2. Gas Recycling

While models for star formation and feedback are ubiquitous in the current generation of numerical simulations, it is much less common to include the recycling of mass and metals which are lost from evolving stellar populations, a fundamental process in the enrichment of the interstellar and intergalactic mediums. The few models that do include this "gas recycling" typically do so in a continuous fashion, during which, at every time step, a small fraction of mass and metals is transferred from a single stellar particle to a set of nearest SPH neighbors (e.g., Steinmetz & Mueller 1994; Kawata 2001; Kawata & Gibson 2003; Okamoto et al. 2005; Scannapieco et al. 2005; Stinson et al. 2006; Tornatore et al. 2007; Wiersma et al. 2009; Montuori et al. 2010; Perez et al. 2011). This approach can accurately track the spatial and temporal distribution of mass and metals at a reasonable computational cost, but unfortunately, because particles can exchange mass with many neighbors, at many different times, it is impossible to trace the exact origin of any particular mass or metal element.

Given a desire to unambiguously track the origin and evolution of interstellar metals, the work presented here adopts a stochastic approach to gas recycling (e.g., Lia et al. 2002; Martínez-Serrano et al. 2008). This less-used approach is designed to mirror the stochastic star formation scheme that is typically implemented in numerical simulations. While stochastic star formation probabilistically converts SPH particles into a fixed number of collisionless stellar particles based upon the
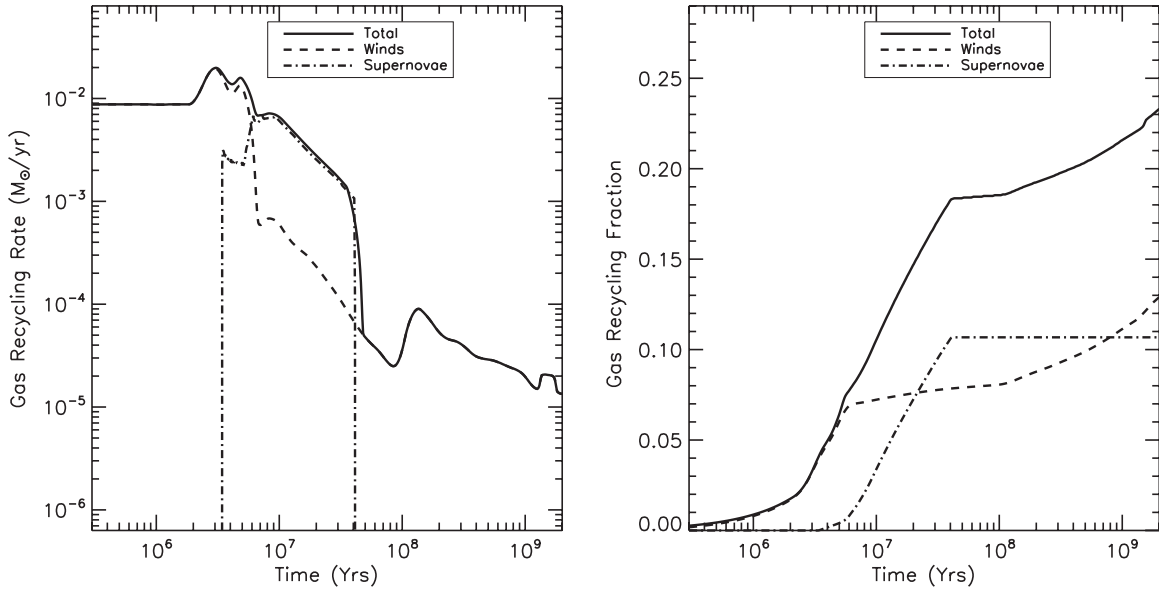
Figure 1. Mass recycling rate (left) and integrated mass recycling fraction (right) from a Starburst99 model for a $10^6 \, M_\odot$ stellar population with a Kroupa IMF.

star formation rate, our stochastic gas recycling converts stellar particles into SPH particles based upon theoretical mass return rates for a simple stellar population. When used in conjunction, these methods can accurately track the temporal and spatial interchange of baryonic material between stellar populations and the ISM, a necessary element to any study of the evolution of interstellar metals.

In our stochastic approach, the probability of turning an individual star particle into an SPH particle at any given time step is given by

$$p_{\rm recy} = \left[1 - \exp\left(-\frac{\Delta t}{t_{\rm recy}} \right) \right], \quad (5)$$

where Δt is the current simulation time step, and

$$t_{\rm recy} = \frac{M_*(t)}{dM_{\rm gas}/dt}. \quad (6)$$

Here, $M_*(t)$ is the expected stellar mass at time t and $dM_{\rm gas}/dt$ is the mass return rate at the same time. While the physical mass of the stellar particle in the simulation remains constant, the expected stellar mass identifies the amount of mass that would have been returned to the ISM if we implemented continuous gas recycling. We should make clear that there are no hybrid particles in the simulation, so the expected stellar mass has no influence on the simulations dynamics. It is necessary, however, for Equation (6) to use the expected stellar mass in order for the stochastic recycling routine to reproduce the desired Starburst99 gas recycling rate in the simulations.

In practice, the simulation selects a random number between 0 and 1, and performs the particle conversion if this number is less than $p_{\rm recy}$. We calculate the mass return rate, $dM_{\rm gas}/dt$, directly from Starburst99 synthetic population models (Leitherer et al. 1999; Vázquez & Leitherer 2005; Leitherer et al. 2010). These models include gas recycling contributions from core-collapse supernova and AGB winds, but do not include contributions from Type Ia supernovae. At each time step, stellar particles are assigned a mass return rate determined by their age, metallicity, and an initial mass function (Υ). For the simulations presented here, we choose a Kroupa initial mass function (IMF) with

solar metallicity. The resulting mass return rate and mass return fraction are demonstrated in Figure 1.

While it will be fruitful to explore variations in the mass return according to varying IMF assumptions, real-time metallicity information, or even easily parameterized functional forms of mass return that include Type Ia supernovae (see, e.g., Jungwiert et al. 2001; Leitner & Kravtsov 2011) we choose to allow variations in mass return through a simple scale factor to the return rate shown in Figure 1. Specifically, we define a scalar, ζ, and employ a mass return rate normalized as such

$$\frac{dM_{\rm gas}}{dt} = \left(\frac{\zeta}{\frac{1}{M_*} \int_0^\infty f_{sb99}(t, Z, \Upsilon) dt} \right) f_{sb99}(t, Z, \Upsilon), \quad (7)$$

where $f_{sb99}(t, Z, \Upsilon)$ is the mass return rate from Starburst99 as shown in Figure 1. The expected stellar mass in Equation (6) is then calculated as

$$M_*(t) = M_0 - \int_0^t \frac{dM_{\rm gas}}{dt'} dt', \quad (8)$$

where M_0 is the original mass of the stellar particle. We note that for large values of ζ, and for old stellar ages, $M_*(t)$ can become negative, yielding unphysical negative values for $t_{\rm recy}$ and consequently a negative probability $p_{\rm gas}$. This situation is non-catastrophic, however, because, in practice, it leads to an immediate conversion of this stellar particle to SPH.

The parameter ζ allows us to control the timescale and efficiency of gas recycling. For example, the Kroupa IMF we employ dictates that 37% of the stellar mass will be returned to the ISM after 10 Gyr. Setting $\zeta = 0.37$ makes the normalization unity and the recycling therefore tracks exactly what is shown in Figure 1. Setting $\zeta = 1$ will produce complete (i.e., 100%) recycling of the stellar mass within 10 Gyr, while $\zeta = 100$ effectively yields the instantaneous recycling approximation with all the stellar mass being returned within $\sim 3 \times 10^6$ years. Finally, and perhaps obviously, setting $\zeta = 0$ turns off recycling altogether giving us the flexibility to study the impacts of varying amounts of recycling on metallicity evolution.

When a star particle is returned to the gas phase, the particle type is instantly converted from stellar to gas at the end of the

current time step. The fields which are defined for both SPH particles and star particles, such as the position, velocity, mass, metallicity, etc., remain unchanged during the conversion. For concreteness, the metallicity of a particle remains unchanged during the transition to or from the stellar state. The metallicity increases while in the gas phase (according to Equation (9)), but remains fixed while in—or making transitions to and from—the stellar state.

SPH quantities must be initialized for the newly converted gas particle. In principle, we could set these fields to properly reflect the physical state of the gas being returned and explore the feedback implications that naturally result from this gas recycling model. However, in practice, we are resolution-limited, we already included feedback according to the SH03 model, and our primary concern is representing the overall mass budget faithfully. To this end, we give a newly formed SPH particle properties that will allow it to quickly homogenize into the surrounding medium. In particular, the entropy is set equal to that of gas at a temperature of T = 50,000 K and a density (chosen to be the star formation critical density) of $\rho = 0.5$ cm^{-3}. It is important to note that our simulations are nearly invariant to our choice of these values. Changing the initial entropy by an order of magnitude in either direction yields no obvious differences in the simulations. In effect, this implementation of gas return serves to provide a passive source of gas for our evolving system, without providing strong feedback.

During both star formation and gas recycling events, no particle splitting occurs. As such, the total number of baryon particles (stars and gas) is conserved throughout the simulation. Effectively, baryon particles are permitted to flip back and forth between the gas and stellar phases, according to the star formation and gas recycling rates. Because baryon particle number is conserved and no mass is transferred between particles, mapping a particle's initial position to a final position a trivial task, regardless of the number of times it was turned into a star particle or returned to the gas phase. Using this stochastic gas recycling method provides the distinct advantage that we can retrace all mass to a unique initial position regardless of the star formation or gas recycling history.

2.3. Metallicity Enrichment

We implement a method for calculating the metal enrichment based on the instantaneous star formation rate to determine the metallicity enrichment rate. Unlike star formation, galactic winds, and gas return, metal enrichment is carried out in a continuous fashion, where the metal formation rate is given by

$$\frac{dM_Z}{dt} = y \frac{dM_*}{dt} \qquad (9)$$

and y is the metal yield and dM_*/dt is the instantaneous star formation rate. For our simulations, we use a fixed yield of $y = 0.02$. The metallicity will increase wherever there is ongoing star formation, as determined via the SH03 star formation model. As such, diffuse gas will not be star forming and will therefore not enrich (see SH03 for details). The scalar metallicity is updated at each time step using an Eulerian integration scheme. This scalar metallicity does not track-independent species, but instead provides a single metallicity value proportional to the integrated star formation rate. This metal enrichment scheme is strictly independent of our gas recycling routine.

The metallicity enrichment does not affect the evolution of the simulation because there are no metallicity-dependent

dynamical processes included, such as metal line cooling. Because no mixing is allowed, nearby particles may have large metallicity variations. This is not problematic, as long as we interpret the metallicity at a given location to be a kernel-weighted average of nearby particles, as is traditional for determining fluid quantities in SPH. Mixing would homogenize the individual particle metallicities, while leaving the average value of the kernel-weighted metallicity unchanged.

Using this enrichment scheme, we are able to cleanly decompose the metallicity of an SPH particle into contributions from its initial metallicity and star formation history. More important, we are able to scale our metal yield and modify our initial metallicity setup in our post-processing analysis, without requiring additional simulations. This is possible because all of the gas content of an SPH particle has an unambiguous and unique initial location and star formation history, which is not true when particle mass mixing is used. In later sections, our ability to arbitrarily modify initial metallicity gradients of our progenitor galaxies is critical in allowing us to thoroughly sample the range of metallicity gradients of our progenitor galaxies, without large computational requirements.

3. ISOLATED GALAXIES

In our analysis, we take the nuclear region of a galaxy to be a sphere of radius 1 kpc about the galactic center. We determine the nuclear metallicity from the star formation rate weighted average of all gas particles inside this sphere. A 1 kpc spherical region is used for consistency with the observations of Kewley et al. (2006). However, it should also be noted that our results would not fundamentally change for slightly larger or smaller definitions of the nuclear region.

We use star formation rate weighted averages to mimic observations of H II regions, which naturally select star-forming gas. Unless otherwise stated, all nuclear metallicities quoted in this paper are gas phase and star formation rate weighted. In particular, the central depressions in gas-phase metallicity presented here should not be confused with enhancements in stellar metallicity seen in late-stage mergers and relaxed elliptical galaxies. These increases in stellar metallicity are relics from the merger-driven starbursts that leave behind central stellar cusps in merger remnants (Mihos & Hernquist 1994a; Hopkins et al. 2008) and elliptical galaxies (Hopkins et al. 2009a, 2009c). These starbursts occur at late stages in a merger, following coalescence, from enriched, star-forming gas, yielding a central population of young, metal-enhanced stars (see, e.g., Figures 27 and 28 in Hopkins et al. 2009a).

The star formation rate weighted nuclear metallicity is defined as

$$\bar{Z} = \frac{\int_V \dot{\rho}_* (\vec{r}) \, Z (\vec{r}) \, dV}{\int_V \dot{\rho}_* (\vec{r}) \, dV}, \qquad (10)$$

where $\dot{\rho}_* (x, y, z)$ is the star formation rate density, $Z (x, y, z)$ is the fraction of gas mass in metals, and the integral is performed over the 1 kpc spherical region about the galaxy's center. The star formation rate density is calculated as

$$\dot{\rho}_*(\vec{r}) = \sum_j \frac{dM_{*,j}}{dt} W(|\vec{r} - \vec{r}_j|, h_j), \qquad (11)$$

where $W(|\vec{r} - \vec{r}_j|, h_j)$ is a smoothing kernel function, h is a smoothing length, and dM_*/dt is a particle's instantaneous star formation rate (discussed in Section 2.1). For our analysis, we use a galaxy's central black hole to define the galactic center;
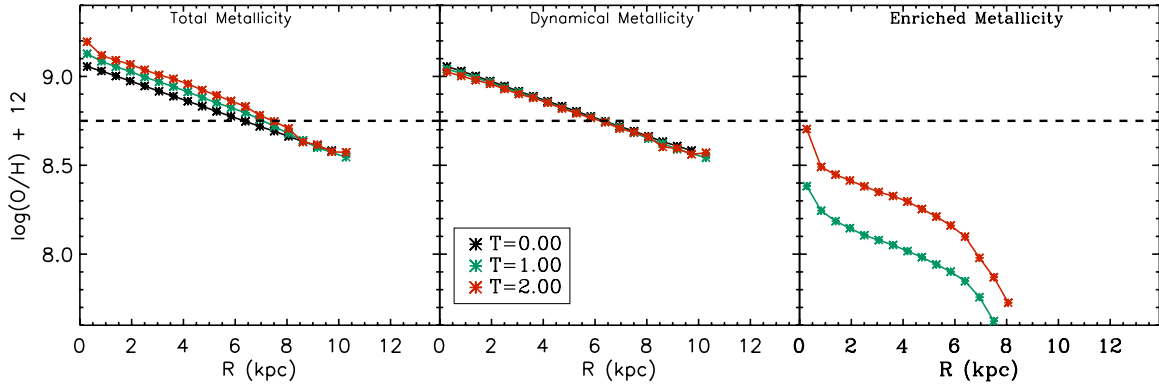
Figure 2. Metallicity profiles for the "C" isolated galaxies evolved for 2 Gyr. The total (left), dynamical (center), and enriched (right) metallicities are shown separately. The horizontal dashed line denotes the mean initial metallicity for the disk. The stability of the dynamical metallicity indicates that radial gas flows are minimal in our isolated systems, while the total metallicity gradient increases over time owing to chemical enrichment. A clear distinction is made between the dynamical metallicity, which is a product of our initial conditions, from the enriched metallicity, which is a product of ongoing star formation in the simulation.

(A color version of this figure is available in the online journal.)

Table 1
Progenitor Disk Properties

Disk Identifier	Total Halo Mass ($M_\odot$)	Initial Stellar Mass ($M_\odot$)	Initial Disk Gas Fraction	h (kpc)	$N_{\rm Halo}$	$N_{\rm gas}$	$N_{\rm stars}$
A	2.3×10^{11}	1.1×10^{10}	10%	2.4	532,500	30,000	145,500
B	5.1×10^{11}	2.4×10^{10}	10%	3.2	532,500	30,000	145,500
C	9.5×10^{11}	4.4×10^{10}	10%	3.9	532,500	30,000	145,500
D	13.5×10^{11}	6.2×10^{10}	10%	4.4	532,500	30,000	145,500
C2	9.5×10^{11}	4.0×10^{10}	20%	3.9	532,500	40,000	135,500
C3	9.5×10^{11}	3.2×10^{10}	40%	3.9	532,500	60,000	115,500
C4	9.5×10^{11}	2.4×10^{10}	60%	3.9	532,500	80,000	95,500

however, our results are unchanged if we use the potential minimum or any other reasonable measure of the galactic center. This approach neglects projection effects, but instead provides information about the "true" nuclear region.

The metallicity of each SPH particle consists of two separate contributions: an initial metallicity and an enriched metallicity. The initial metallicity of an SPH particle is completely determined by the particle's initial radial position (discussed in Section 3.1) and is unchanging in time, while the enriched metallicity grows owing to star formation. The metallicity of an SPH particle as a function of time is given by

$$Z_{\rm gas}(t) = Z_{\rm init} + \frac{y}{M_{\rm gas}} \int_0^t \frac{dM_*(t')}{dt'} dt', \qquad (12)$$

where $dM_*(t')/dt'$ is the particle's complete time-dependent star formation rate history. The integration of the rightmost term in Equation (12) should be carried out starting at the beginning of the simulation (i.e., $t = 0$), regardless of whether a particle has been recycled or not. Since $dM_*(t')/dt'$ is non-zero only when a particle is actively star forming (i.e., in the gas state and above the star formation threshold density), periods of time when a particle is in the stellar state or below the star formation threshold density (see Section 2.1) will not contribute to Equation (12).

The metallicity of the nuclear region is calculated similarly to the metallicity of an individual SPH particle, with an additional sum over an ensemble of particles weighted by their star formation rates. We explicitly break the nuclear metallicity into two components,

$$\bar{Z} = \frac{\sum_i Z_{i,\rm init} \dot{M}_{*,i}}{\sum_i \dot{M}_{*,i}} + \frac{\sum_i Z_{i,\rm enrich} \dot{M}_{*,i}}{\sum_i \dot{M}_{*,i}}, \qquad (13)$$

where the sum is performed over the particles that fall within the nuclear region. The first term contains the contribution from the initial metallicity gradient of our progenitor galaxies while the second term contains the contribution from star-formation-induced metallicity enrichment. For clarity throughout, we call the first term the "dynamical metallicity," as it is a dynamical result of the initially assumed metallicity gradient, while we call the second term the "enriched metallicity," as it is a product of metal enrichment. For concreteness, the metallicity gradients for one of our "C" isolated galaxies evolved in isolation for 2 Gyr is shown in Figure 2 with contributions from the dynamical and enriched components explicitly shown (see Section 3.2).

3.1. Isolated Galaxy Setup

The isolated galaxies used in this paper are modeled following the analytical work of Mo et al. (1998) employing the procedure outlined in Springel et al. (2005). Our fiducial galaxy consists of a dark matter halo, an embedded rotationally supported exponential disk, a stellar bulge, and a central supermassive black hole.

We construct a set of four isolated galaxies with total system masses ranging from $\sim 10^{11}\ M_\odot$ to $\sim 10^{12}\ M_\odot$, as outlined in Table 1. Although varied in mass, all systems are constructed to be self-similar in order to isolate the effects of mass from other quantities that may correlate with mass in observed systems. The total mass of the disk (stars and gas combined) is chosen to be a constant fraction (4.0%) of the halo mass for all progenitor galaxies, with four settings for the initial gas fraction (8%, 20%, 40%, and 60%). All halos have spin parameters equal to $\lambda = 0.05$, which effectively sets the disk radial scale length. The initial stellar disk scale height is set to a fixed fraction (0.2)
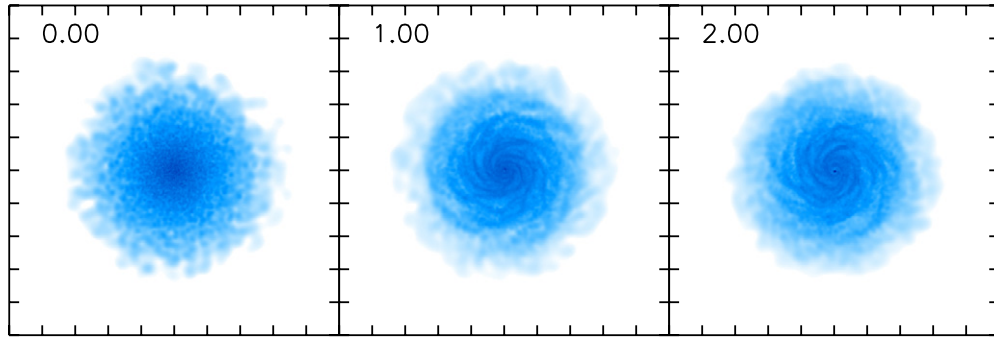
Figure 3. Gas surface density is shown for our isolated "C" disk evolved for 2 Gyr. The disks evolve stably and without bar formation or significant radial gas inflow for 2 Gyr.
(A color version of this figure is available in the online journal.)

of the initial disk scale length, while the gaseous scale height is determined by satisfying hydrostatic equilibrium (Springel et al. 2005). Stellar bulges are included as part of the fiducial galaxy setup and are given a fixed fraction (1%) of the system mass. The resulting disk setup has a Toomre Q parameter that varies as a function of galactocentric radius, but is everywhere greater than unity—indicating stability against axisymmetric perturbations.

The dark matter halos follow Hernquist (1990) profiles with concentration indices of $c = 10$. The stellar and gaseous disk components are modeled with exponential surface density profiles,

$$\Sigma_{*,g}(r) = \frac{M_{*,g}}{2\pi h^2} \exp\left(-\frac{r}{h}\right), \qquad (14)$$

where $M_{*,g}$ is the total mass of stars and gas in the disk, respectively, and h is their common scale length set by the disk's angular momentum (Mo et al. 1998; Springel & White 1999). Stellar bulges are taken to be spherical Hernquist (1990) profiles, where the bulge scale length is given in terms of the halo scale length, $a_b = 0.2a$, and the bulge mass fraction to be 1% of the halo mass.

The initial metallicity profile of our progenitor galaxies enters as an assumption. We model the metallicity profile of the disk as an exponential,

$$Z(r) = Z_0 \exp\left(-\frac{r}{h_z}\right), \qquad (15)$$

where the central metallicity, Z_0, and the metallicity scale length, h_z, are chosen to be consistent with observations. Isolated galaxies show dispersion in their radial metallicity gradients. We could include this dispersion in our simulations by adding in a Gaussian error term to Equation (15); however, no dispersion is used when setting the initial metallicity profile for our isolated galaxies because this would add an extra element of uncertainty into our models and add noise to our results, without yielding systematic changes or further insight.

We assume that oxygen makes up 30% of the metals by mass. The constant oxygen mass fraction is a necessary assumption of our models, because we track only one scalar metallicity value. We note that our results are not particularly sensitive to our choice of the oxygen mass fraction, since this is merely a normalization of the overall metallicity.

We fix the central metallicity values to the observed relation of Tremonti et al. (2004) so that the central metallicity is given in terms of the stellar mass:

$$12 + \log(O/H) = -1.492 + 1.847x - 0.08026x^2, \qquad (16)$$

where $x = \log_{10} M_*$. Initially, we use the exact value given by Equation (16) when discussing the process of nuclear metallicity evolution in Section 4. However, in Section 5 we pick the central metallicity of each progenitor galaxy from a Gaussian distribution with a standard deviation, $\sigma = 0.1$ dex, taken from Tremonti et al. (2004). Similarly, we use the average result from Zaritsky et al. (1994) of $h_z = h/0.2$ in Section 4. However, in Section 5 we pick the slope of the metallicity gradient from a Gaussian distribution with a standard deviation of $\sigma = 0.3h_z$.

3.2. Isolated Galaxy Evolution

While the metallicity evolution of isolated galaxies is not the focal point of this paper, we take a moment in this section to demonstrate that our galaxy models are indeed stable and evolve very little in isolation. We specifically demonstrate that the galaxy models do not develop strong bars since these structures can lead to significant radial inflows of gas. Such processes obscure the true origin of any central metallicity evolution and what is specifically a result of the merger.

The evolved gas surface density, seen in Figure 3, demonstrates that our disks are both stable and free of strong bars over at least 2 Gyr, the typical duration of the galaxy major mergers we study. As a result, the metallicity gradients of our isolated systems evolve very little, as seen in Figure 2. We further demonstrate the characteristics of our isolated disks in Figure 4 where we show the star formation rates and gas fractions for the C2, C3, and C4 systems.

To understand where the small amount of metallicity evolution does come from, Figure 2 also shows the evolution of the initial metallicity gradient or the "dynamical" metallicity (middle panel), and the contribution from ongoing star formation or the "enriched" metallicity (right panel). From this information, it is easy to see that the small increase in central metallicity and gradient is a result of chemical enrichment from ongoing star formation, while the initial metallicity gradient remains nearly unchanged.

Motivation to emphasize the stability of our initial disk models stems from the fact that the disks used in previous studies (e.g., Montuori et al. 2010) appear to be bar unstable over short timescales (see their Figure 2 in their Appendix). These bars result in strong radial mixing and a flattening of their radial metallicity profiles (see Figure 1 in their Appendix). While bar-induced gas inflows are indeed a valid physical mechanism for modifying the nuclear metallicity, we wish to eliminate this complication from our study to make our results easier to interpret.
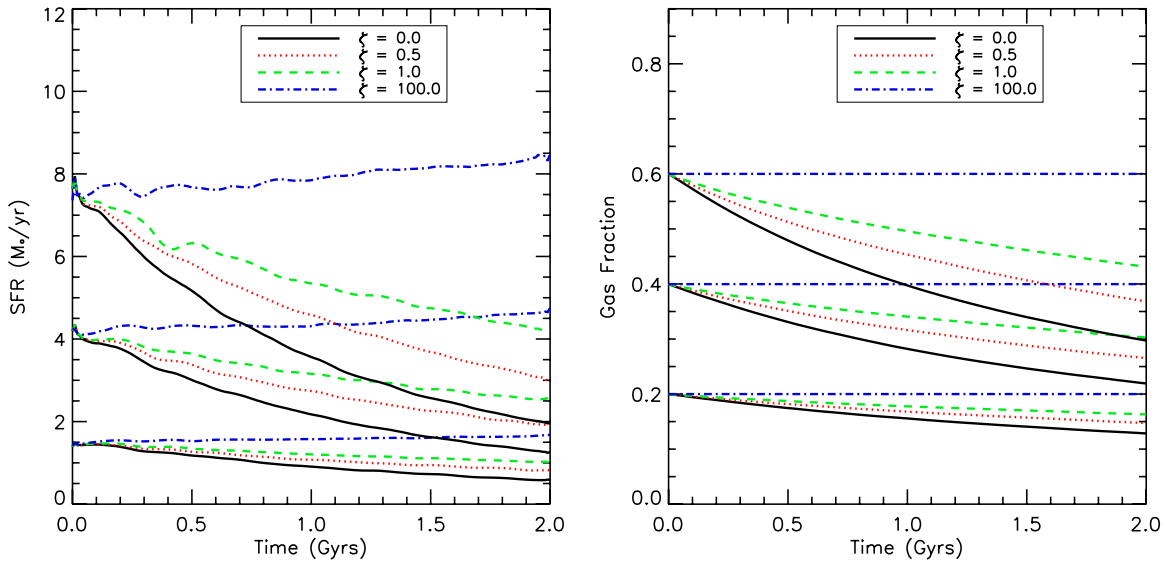
Figure 4. Star formation rates and gas fractions for the C2, C3, and C4 systems evolved for 2 Gyr with varying gas recycling parameters. The gas return parameters, identified in the legend, are varied from $\zeta = 0.0$ (i.e., no gas recycling) to $\zeta = 100.0$ (i.e., nearly instantaneous recycling). Unless otherwise noted, subsequent sections and simulations use $\zeta = 0.3$, which is the unscaled value taken from the Starburst99 simulations.

(A color version of this figure is available in the online journal.)
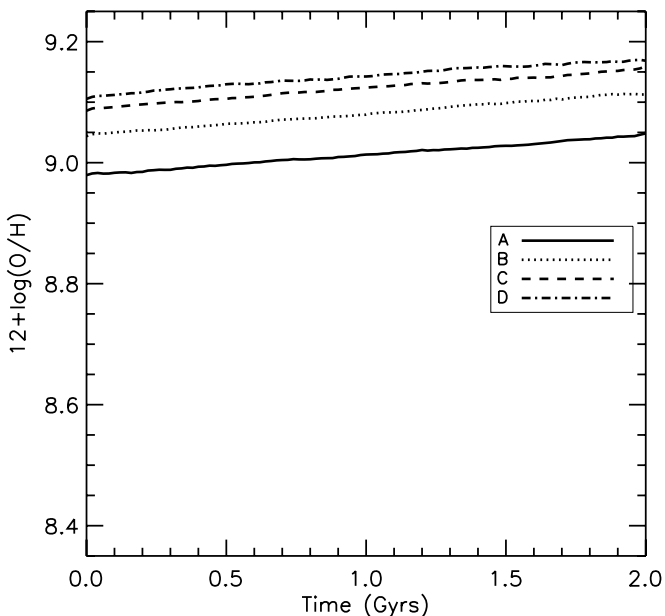
Figure 5. Nuclear metallicities for the A, B, C, and D, isolated galaxies evolved for 2 Gyr are shown. The nuclear metallicity of our isolated model galaxies increases monotonically with time owing to chemical enrichment, as demonstrated in Figure 2.

The evolution of the nuclear metallicity of the four progenitor disks, described in Table 1, is demonstrated in Figure 5. The nuclear metallicity of all isolated disks is well described by a mild and monotonic increase over at least 2 Gyr. The steady behavior of the isolated galaxy nuclear metallicity ensures that any strong changes during the merger simulations are a product of the merger process, rather than disk instability.

While exploring the behavior of isolated disks, we can also demonstrate the effects and capabilities of stochastic gas recycling. When evolving the "C" systems (i.e., C2, C3, and C4 from Table 1), we vary the gas recycling parameter and examine the resulting gas fraction and star formation rate evolution.

The results, shown in Figure 4, demonstrate that the gas is locked into stars more efficiently when the gas recycling parameter is small. As a result, the star formation rates, which largely depend on the amount of gas available for star formation, are consistently larger for increasing values of the gas recycling parameter. Simulations that use efficient gas recycling maintain larger gas fractions and star formation rates throughout the simulation.

In the limit of very large gas recycling parameters, all newly formed stellar material is quickly returned to the ISM. As a result, the gas fraction for large gas recycling parameters stays nearly constant. The corresponding star formation rates slowly increase as gas naturally cools and condenses over time.

4. MERGING GALAXIES

While keeping all of the conventions for nuclear metallicity defined in Section 3, we now consider the evolution of galactic nuclear metallicity for merging systems. Since our interacting systems are spatially extended and overlap substantially during the interaction, they do not follow Keplerian trajectories. However, we use the terminology of Keplerian orbits to clearly describe the merger setup.

To completely specify our merging setup, we must specify the properties of the merger orbit (two parameters) and the relative orientation of each galaxy with respect to the orbit (two parameters for each galaxy). We start by specifying that the systems will be on zero energy orbits (i.e., eccentricity value of unity for Keplerian objects). The orbital angular momentum is then set by picking a value for the impact parameter, assuming Keplerian trajectories (the "real" impact parameter found in the simulations will be larger than this value). We hold the impact parameter fixed (5 kpc) for all simulations. The spin angular momentum vector of each galaxy is varied with respect to the orbital angular momentum vector according to the orientations detailed in Table 2 as visually depicted in Figure 6.

The parameter space of mergers is quite large. To explore this parameter space, without using an excessively large number of simulations, we first perform a detailed exploration of a single case. We then systematically vary merger parameters, such as
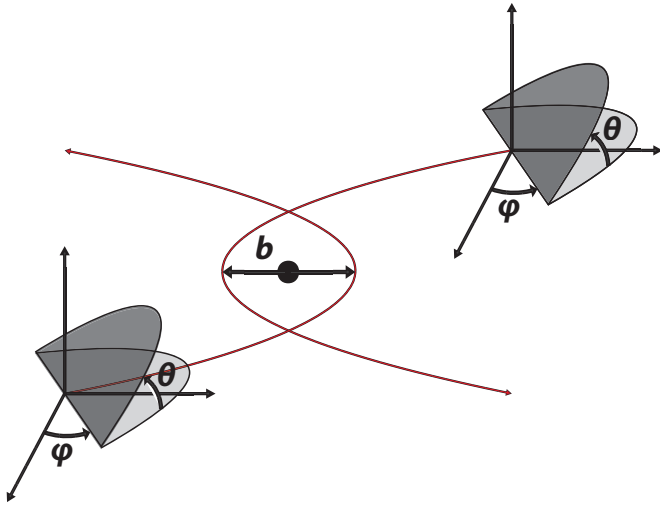
Figure 6. Schematic representation of the merger setup. Our coordinate system is defined by the plane of the merger orbit, and each disk's orientation is independently adjusted with respect to this plane.

(A color version of this figure is available in the online journal.)

Table 2
Orbital Orientations

Orientation Identifier	θ_1 (deg)	ϕ_1 (deg)	θ_2 (deg)	ϕ_2 (deg)
a	90	90	0	0
b	180	0	0	0
c	180	0	180	0
d	90	0	0	0
e	30	60	−30	45
f	60	60	150	0
g	150	0	−30	45
h	0	0	0	0
i	0	0	71	−30
j	−109	90	71	90
k	−109	−30	71	−30
l	−109	30	180	0
m	0	0	71	90
n	−109	−30	71	30
o	−109	30	71	−30
p	−109	90	180	0

the disk orientation, progenitor disk mass, merger mass ratio, orbital angular momentum, and so forth. While this does not necessarily cover all of merger parameter space, it does enable us to paint a coherent picture detailing the relation between the evolution of the merger and the evolution of the nuclear metallicity.

We select our fiducial galaxy merger to be two identical "B" disks merging on the "e" trajectory (see Tables 1 and 2). This setup is neither average nor special and is simply selected to demonstrate in detail the relationship between the merger state and evolution of the nuclear metallicity. While Section 4.1 is restricted to understanding a single merger evolution, Sections 4.2–4.4 show that much of the nuclear metallicity evolution can be understood in terms of generic merger properties that will continue to drive the nuclear metallicity evolution as we move beyond this fiducial setup.

4.1. Metallicity Evolution in Merging Systems

In stark contrast to the isolated systems presented in Section 3.2, the nuclear metallicity of interacting galaxies is
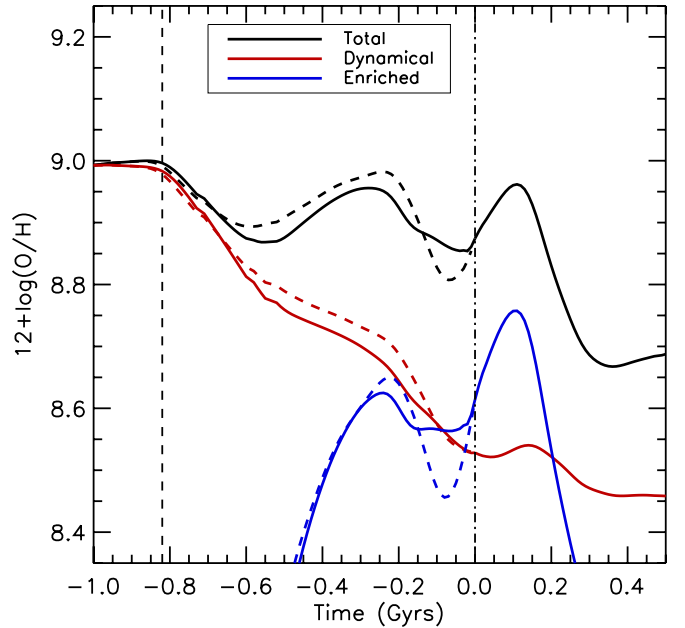
Figure 7. Total (black), dynamical (red), and enriched (blue) nuclear metallicities as a function of time for the "BBe" merger simulation. The two disks, which do not have identical metallicity evolutionary tracks, are distinguished by the solid and dashed lines. First pericenter passage and final coalescence are marked with vertical dashed and dot-dashed lines, respectively.

(A color version of this figure is available in the online journal.)

a complicated function of time, as shown in Figure 7. Moreover, there is a clear change in the evolutionary behavior of the nuclear metallicity following pericenter passage when the disks stop behaving like isolated systems and enter a period of evolution dominated by the merger dynamics.

Before delving further into the merger details, we note that there is a characteristic "double dip" shape to the nuclear metallicity evolution. This is caused by the ongoing competition between metallicity dilution and chemical enrichment. While the exact evolutionary track shown here is specific to this particular merger setup, the characteristic double dip in the metallicity will appear repeatedly in many other cases. In general, galactic close passages lead to gas inflows (yielding inflows of low-metallicity gas) which are quickly followed by star formation (yielding chemical enrichment).

During the period of time between first pericenter passage and final coalescence, the nuclear metallicity evolution is driven by (1) radial inflows of low-metallicity gas caused by the tidal interaction, (2) chemical enrichment caused by star formation activity, (3) locking of metals and gas in the stellar phase, and (4) removal of gas and metals via galactic winds. The combined effect of these four mechanisms, which are discussed in detail in the following sub-sections, determines the relative importance of metallicity dilution and chemical enrichment, which ultimately decide when and where the nuclear metallicity will be diluted or enhanced.

4.1.1. Metallicity Dilution and Chemical Enrichment

The influence of radial gas inflows and chemical enrichment are demonstrated in Figure 8, which shows the galactic separation, rate of change of nuclear metallicity, nuclear star formation rate, and nuclear gas inflow rate. In terms of basic merger properties, there is an influx of gas following first pericenter passage and periods of gas inflow associated with each additional close
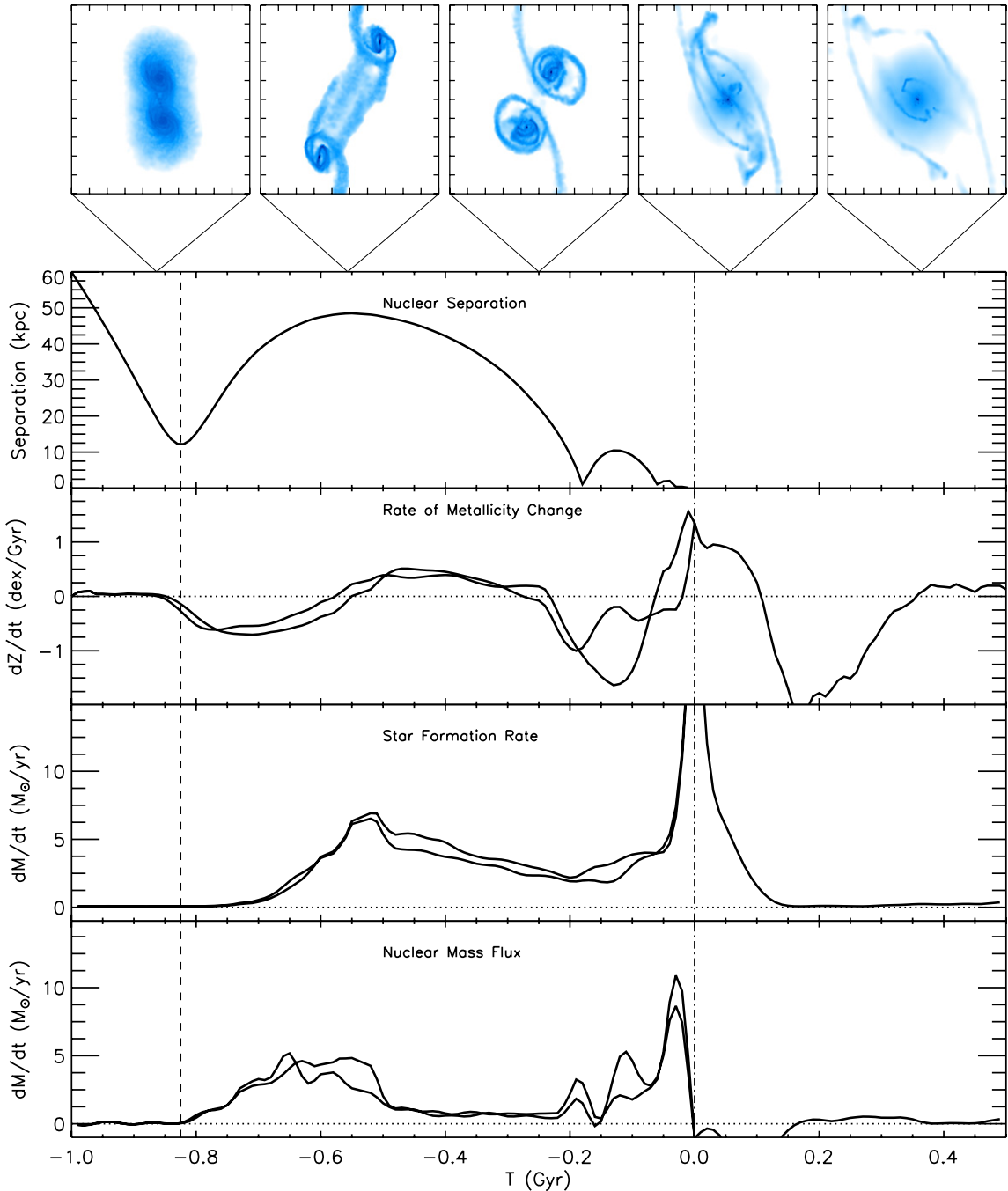
Figure 8. Several diagnostics for assessing the metallicity evolution of our fiducial merging system are shown. The top row shows contour plots of the gas density, with lines indicating the stage of the merger. From top to bottom, the subsequent time series show the galactic nuclear separation, the rate of change of the nuclear metallicity, nuclear star formation rate, and nuclear gas inflow rate. Pericenter passage and final coalescence are denoted by dashed and dot-dashed lines, respectively. In general, periods of ongoing nuclear metallicity dilution can be associated with strong nuclear gas inflows, while times of ongoing nuclear metallicity enhancement are associated with high nuclear star formation rates.

(A color version of this figure is available in the online journal.)

passage. These gas inflows give rise to high nuclear star formation rates. While these previous points have been studied extensively in other papers (Barnes & Hernquist 1991, 1996; Mihos & Hernquist 1994b, 1996; Iono et al. 2004), we instead focus here on the influence that these generic merger properties have on the evolution of the nuclear metallicity. Specifically, times of strong gas inflow correspond to periods of nuclear metallicity depression, while high star formation activity aligns with

nuclear metallicity enhancement. These qualitative relationships remain true as the merger parameters are varied.

Previous studies have found that the depression in the nuclear metallicity is correlated with the mass of gas that migrated to the nuclear region (Rupke et al. 2010a). This result is reproduced in our simulations when we neglect star formation (similar to the red line in Figure 7) and is a clear-cut demonstration of metallicity dilution. However, when we also consider contributions

from chemical enrichment and the consumption of gas via star formation, this correlation disappears.

Inspection of Figure 8 shows that, in general, periods of strong gas inflow occur simultaneously with times of ongoing nuclear metallicity depression. Similarly, periods of high star formation give rise to enhancements in the nuclear metallicity. Interestingly, neither the nuclear star formation rate nor the nuclear mass inflow rate correlate well with the rate of change of the nuclear metallicity because they exchange roles playing the dominate driver of the nuclear metallicity throughout the merger. The reason is that metallicity dilution, chemical enrichment, locking of gas in the stellar phase, and galactic winds all influence metallicity evolution. While more involved parameters (e.g., the difference between the star formation and nuclear mass inflow rate) yield better, albeit imperfect, correlations, these trends can be misleading and they tend to overcomplicate a fairly simple point. In particular, changes to the nuclear metallicity at any time during the interaction can be understood by examining the nuclear star formation and gas inflow rates. Furthermore, the nuclear star formation and gas inflow rates are naturally explained via the well-studied merger process.

From this single merger example, it seems plausible that the role of metallicity dilution and chemical enrichment are natural consequences of the merger process. However, by inspection of Figure 7, neither effect is overwhelmingly dominant. Hence, in the following analysis we pay attention not only to metallicity dilution and chemical enrichment, but also effects such as the locking of gas in stars and the launching of galactic winds that work to modulate the efficiency of these processes. Instead of searching for correlations between the changes in the metallicity and these distinct processes, we vary parameters in our simulations to test their influence on the evolution of the nuclear metallicity.

4.1.2. Gas Consumption

Any process that can modify the gas reservoir in the nuclear region can affect the metallicity measurement. Here, we consider the influence of locking gas in the stellar phase when determining the evolution of the nuclear metallicity. Star formation lowers the reservoir of gas in the nuclear region, and hence amplifies the effect of metallicity dilution that occurs when low-metallicity gas floods the central region. While this is definitely a physical effect, its magnitude will be misjudged if the simulations do not properly account for gas recycling. Using the stochastic gas recycling method outlined in Section 2.2, we are able to modulate the efficiency with which gas becomes locked in the stellar phase without changing our star formation efficiency or feedback prescriptions. Instead, we change the gas recycling parameter, allowing gas to be returned from the stellar state back to the ISM.

We first consider a simulation where newly formed stellar material is instantaneously returned to the ISM, such that no gas will be trapped in the stellar phase. At the opposite extreme, we perform a simulation with star formation, but no gas recycling (i.e., $\zeta = 0.0$), which would trap the largest amount of gas in the stellar phase. In between these extremes, we consider three values for the gas recycling fraction, ζ, that show how the nuclear metallicity evolution changes as the efficiency with which gas is locked in the stellar state is varied.

When the gas recycling parameter is set to very large values, the resulting enriched metallicity becomes unphysically high. This occurs when many generations of star formation are allowed to occur over very short timescales as the gas is quickly recycled into the ISM repeatedly. However, the resulting dynamical metallicity remains physical and meaningful, as it describes the change in the nuclear metallicity that will occur as a function of the efficiency with which material is locked in the stellar phase. In fact, dynamical metallicity given by our simulation with instantaneous gas recycling (see the black line in the center panel of Figure 9) is very similar to the results of Rupke et al. (2010a). These simulations capture changes to the nuclear metallicity caused by dilution without any contributions or contamination from the creation of stars. In this case, the nuclear metallicity is well correlated with the mass of gas in the nuclear region, as noted by Rupke et al. (2010a, see their Figure 2). This indicates that the initially high nuclear metallicity is diluted by inflows of low-metallicity gas. However, as the gas recycling parameter is dialed back to lower values, gas is more efficiently trapped in the stellar phase which increases the effect of metallicity dilution.

The simulation with star formation and no gas recycling brackets the upper end for the amount of gas that can be trapped in the stellar phase. In this case, the dynamical metallicity (red dotted line in the center plot of Figure 9) is lower than the dynamical metallicities of all other simulations and falls ∼0.2 dex below that of the nuclear metallicity with instantaneous recycling. This difference is caused purely by the effect of locking gas in the stellar state. When no gas recycling is used, a substantial fraction of the inner gaseous reservoir is converted into the stellar state, allowing influx of low-metallicity gas to have stronger influences. In addition, the enriched metallicity is lower than any other simulation because the resulting star formation rates are lower when gas is efficiently locked in the stellar state. The resulting total metallicity is below the total metallicity where gas recycling is used.

As gas recycling is included at intermediate values, both the dynamical metallicity and enriched metallicity increase. The increase in the dynamical metallicity for larger gas return fractions is well motivated by the simple physical arguments presented above. Specifically, increasing the gas recycling fraction lowers the efficiency with which gas is depleted from the nuclear region into the stellar state. Hence, as the gas recycling fraction is increased, the mass of gas in the inner reservoir increases and the influence of metallicity dilution is decreased.

The increase in the enriched metallicity for larger gas return fractions is similarly explained. Gas that resides in the nuclear region will tend to remain there for longer periods of time (on average) and achieve higher instantaneous and integrated star formation rates (hence higher metallicities). While this sheds light on the influence of gas recycling, we would like to use physically motivated values for the gas recycling fraction in what follows. We take the unscaled Starburst99 mass return fraction as the fiducial mass return fraction used for the remainder of this paper.

4.1.3. Galactic Winds

Galactic winds are thought to play a leading role in the evolution of the distribution of metals throughout cosmic time. Starburst-driven or AGN-driven winds are ubiquitous phenomena that act to transport metals from the depths of galaxies into the interstellar or intergalactic medium (see, e.g., Veilleux et al. 2005 for a comprehensive review). Galactic winds may also play a prominent role in shaping the MZ relationship (see, e.g., Davé et al. 2007) and because galaxy mergers induce episodes of enhanced star formation, they may also induce periods of
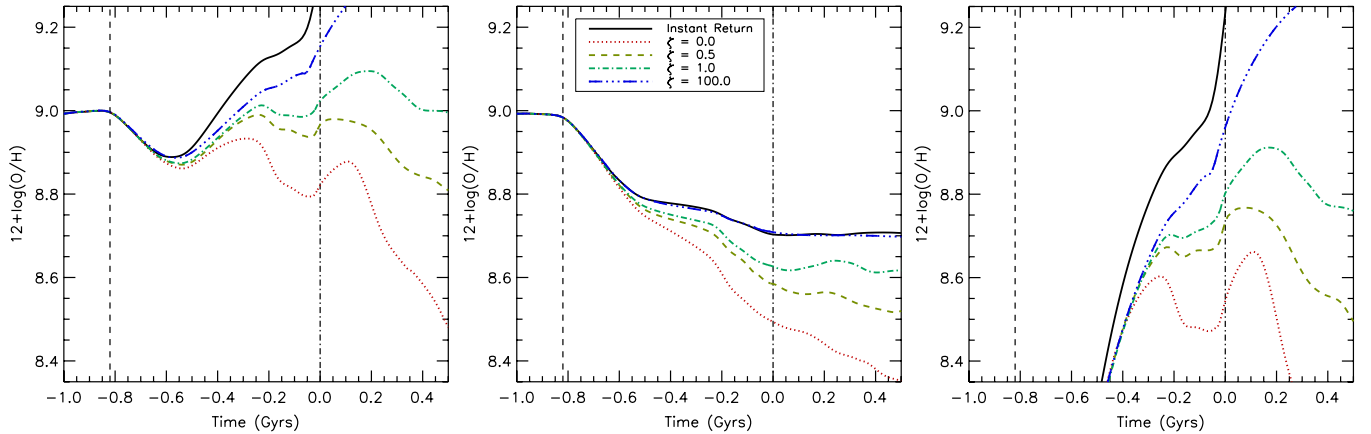
Figure 9. Total (left), dynamical (center), and enriched (right) nuclear metallicities as a function of time for "BBe" merger simulations are shown. The various lines show the nuclear metallicity evolution with several values of the gas recycling coefficient as well as complete and instantaneous gas recycling. For very large values of the gas recycling coefficient (i.e., $\zeta \gg 1$), stellar particles are returned to the gas phase quickly. As the gas recycling coefficient is increased, the results approach the case of instantaneous and complete gas recycling. First pericenter passage and final coalescence are marked with vertical dashed and dot-dashed lines, respectively.
(A color version of this figure is available in the online journal.)
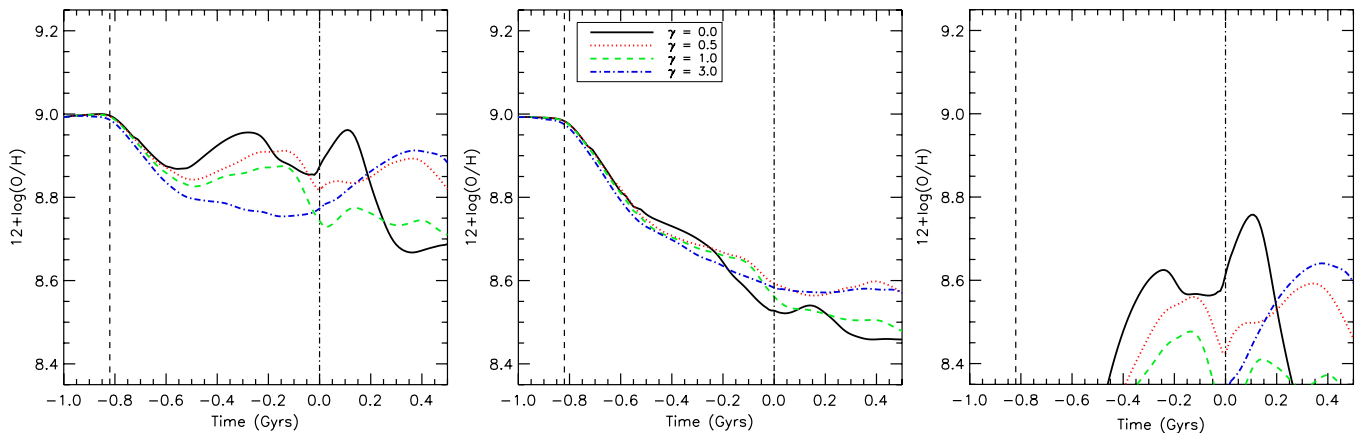
Figure 10. Nuclear metallicities are shown for varied wind launching efficiencies. First pericenter passage and final coalescence are marked with vertical dashed and dot-dashed lines, respectively.
(A color version of this figure is available in the online journal.)

significant feedback and galactic outflows, thereby altering the central metallicity evolution of galaxy mergers.

In the context of this paper, galactic winds can remove gas from central regions and modify the reservoir of material contributing to the nuclear metallicity (Perez et al. 2011). In this capacity, the influence of galactic winds is identical to the locking of gas in the stellar state. To demonstrate the impact of galactic winds on the nuclear metallicity, we present a set of simulations where we vary the mass entrainment, γ. In these simulations we do include gas recycling at the fiducial level, but note that the our conclusions are unchanged if this effect is turned off.

The dynamical metallicity is not substantially affected by galactic winds. Since star formation is already fairly efficient at locking gas in the stellar state, galactic winds provide only an incremental modification to this effect. However, notable changes occur in the enriched metallicity. Specifically, the enriched metallicity is depressed for large values of the mass entrainment because gas with high star formation rates is either quickly converted into the stellar phase or launched in a wind. Therefore, the integrated star formation rates and enriched metallicity values for gas particles remain lower, on average, for higher mass entrainment values.

The resulting nuclear metallicity, shown in Figure 10, is depressed as mass entrainment is increased. This change is primarily caused by changes to the enriched metallicity. However, there is one additional effect that distinguishes galactic winds from locking of material in the stellar phase. While gas that is permanently locked in the stellar state will forever be unable to contribute to the nuclear metallicity or star formation, gas that has been launched in a wind will ultimately fall back onto the disk or even into the nuclear region. We see this effect having an influence in the enriched metallicities of the highest mass entrainment value simulations at late times. Specifically, as gas inflow from previously ejected wind material falls upon the nuclear region, the star formation rates and enriched metallicities are pushed toward higher values.

It should be noted that the galactic wind launching prescription used in this work does not describe a situation where the galactic wind predominately ejects enriched gas. In other words, the metallicity of the wind is the same as the ambient metallicity of the star-forming region from which the wind was launched. This prescription could underestimate the efficiency with which metals are pushed out of a galaxy and into the intergalactic medium. However, this wind launching prescription is straightforward to understand and has the
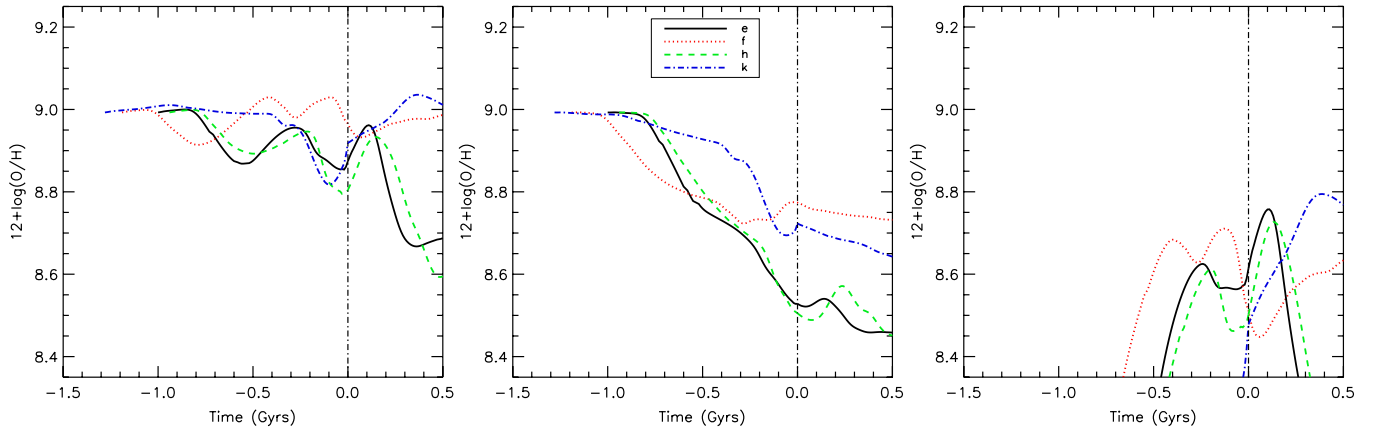
Figure 11. Nuclear metallicity evolution for four identical initial progenitor disks, set on four distinct merging trajectories, all aligned with final coalescence at $t = 0$, as indicated by the dot-dashed vertical line. Each orientation has a unique metallicity evolution, but all share common features. First, depressions of the nuclear metallicity are common following any pericentric passage (though not all pericenter passages induce nuclear metallicity depressions, as demonstrated by the "k" orientation). Second, depressions of the nuclear metallicity are common preceding final coalescence.

(A color version of this figure is available in the online journal.)

direct and notable effect of removing gas from the nuclear region.

Galactic winds do little to change the radial rearrangement of gas which attends a galaxy merger, as shown by the relative insensitivity of the dynamical metallicity to the efficiency of the winds. The only appreciable effects are on the enriched metallicity. In the following analysis, we take $\gamma = 0.3$ as the fiducial mass entrainment value (Rupke et al. 2005).

4.2. Disk Spin Orientation

While the previous analysis focused on a single merger setup, the effect of merger orientation can be tested using a set of identical "B" galaxies merging from 16 orientations (a–p, as detailed in Table 2). All orientations maintain unique metallicity evolutions, as the specifics governing the magnitude and timing of the gas inflows and starbursts are orientation dependent. Here, we will consider which aspects of our fiducial merger's metallicity evolution are found to hold for various merger orientations. To test this, we first examine the metallicity evolution for the four orientations shown in Figure 11.

As is evident from this figure, three of the four disks show strong depressions in their nuclear metallicity following pericentric passage. This is caused by the strong tidal interaction and resulting gas inflows which are a natural byproduct of the merger process. The disk not experiencing a post-pericentric nuclear metallicity depression is identified as being on a nearly retrograde orientation. More concretely, the induced gas inflow following pericenter passage is found to be small compared to the other systems. The idea that some orientations, specifically those on retrograde orbits, have suppressed responses during pericentric passages has been studied previously (Toomre & Toomre 1972; D'Onghia et al. 2010), and we note that the metallicity evolution is affected accordingly in the cases where strong post-pericenter passage responses are not found.

Subsequent depressions in the nuclear metallicity can be identified as occurring during periods of strong gas inflow caused by close encounters. For the "e" and "h" orientations, only one additional close encounter occurs before proceeding to coalescence. However, for the "f" orientation, three metallicity dips can be seen. These metallicity dips are natural products of this particular merger orientation, which leads to three distinct pericenter passages before the galaxies ultimately coalesce. While a hard and fast rule governing the metallicity depression's de-

pendence on merger orientation cannot be given, two statements can be made: most orientations undergo a metallicity depression following pericentric passages (unless the tidal interaction is sufficiently suppressed) and most orientations show metallicity depressions immediately preceding final coalescence. Both of these statements are demonstrated in Figure 11, where three of four (e, f, and h; not k) orientations show post-pericentric dips in their nuclear metallicity and three of four (e, k, and h; not f) orientations show dips in their nuclear metallicities preceding final coalescence.

If we identify the merging time, t_m, to be the time between pericenter passage and final coalescence, we can average the metallicity evolution for several orientations to get an orientation-averaged progression of the nuclear metallicity during the merger. Figure 12 shows the mean nuclear metallicity evolution for all 16 orientations, with the solid region indicating the 1σ variations. Despite the variation that occurs in the nuclear evolutionary tracks for individual orientations, the mean result has a well-defined pattern with reasonably small dispersion and a clear interpretation. Specifically, there are two notable metallicity depressions caused by gas inflows, one following pericentric passage and one preceding black hole coalescence, with a chemical enrichment induced peak separating in between. Also shown in Figure 12 is the average dynamical metallicity. Here, we can see that simulations without chemical enrichment substantially underpredict the resulting nuclear metallicity. However, even when chemical enrichment is included, the mean nuclear metallicity is depressed throughout the interaction.

4.3. Progenitor Masses

We examine the effect that system mass has on the nuclear metallicity evolution using a set of major mergers (i.e., 1:1 mass ratios) with progenitor galaxies of varying mass. As detailed in Section 3.1, the four galaxies used in this paper are constructed to be self-similar. Hence, the mass study performed here isolates the influence of merger mass from other parameters that may scale with mass (e.g., gas fraction, galaxy structure, etc.).

We use four orientations in each mass bin (the "e," "f," "h," and "k" orientations) and average the resulting metallicity evolutionary tracks. The result, shown in Figure 13, is that the
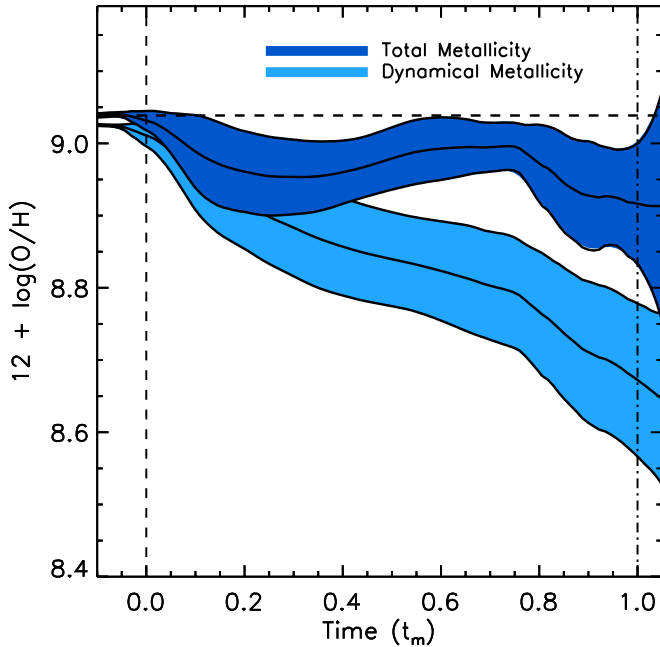
Figure 12. Average metallicity evolution for a set (orientations a–p) of major mergers with identical progenitor galaxies on different merger orientations. The dark blue region denotes the mean nuclear metallicity plus the one sigma variation for BB galaxy mergers on all 16 orientations. The light blue region shows the nuclear metallicity for the same mergers when chemical enrichment from star formation is neglected. First pericenter passage and final coalescence for all orientations are denoted by the vertical dashed and dot-dashed lines, respectively.
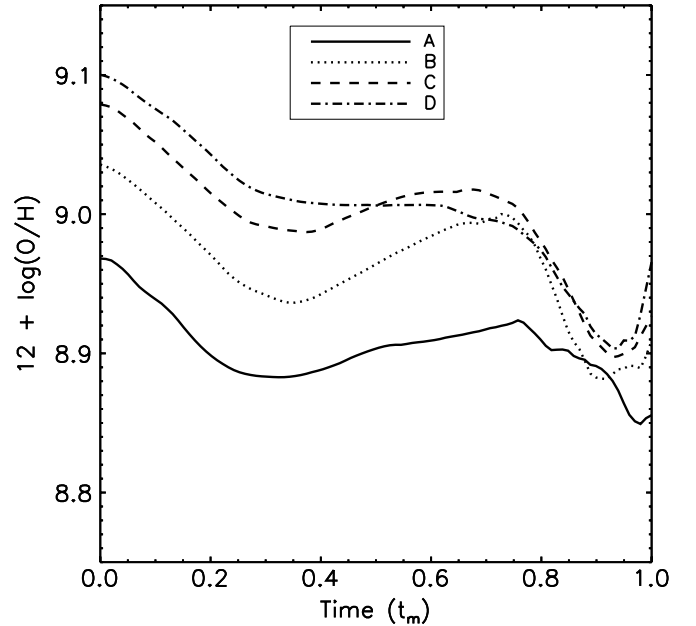
(A color version of this figure is available in the online journal.)

Figure 13. Average metallicity evolution for a set (the e, f, h, and k orientations) of major mergers in four mass bins.

shape of the evolutionary track is nearly preserved, while the magnitude of the depression depends weakly on mass. We note that the preserved shape of the metallicity evolution supports our argument in the previous sections that the metallicity evolutionary track is a natural byproduct of the generic merger process. This indicates that, within the limited range of galaxy masses that are used here, the system mass is not a major consideration in determining the nuclear metallicity evolution.

4.4. Gas Fraction

Initial gas fraction is an important parameter to consider in nuclear metallicity evolution. For higher gas fraction galaxies that, by definition, have lower initial stellar mass, two basic changes occur: the initial nuclear metallicity of the system, as prescribed by the MZ relation, is lowered (decreasing the importance of the dynamical metallicity), and higher star formation rates occur (increasing the importance of chemical enrichment). The combined result, as discussed in this section, is that the nuclear metallicities of interacting systems at higher gas fractions tend to evolve to larger values, rather than decreasing, in contrast to their lower gas fraction counterparts.

We first consider the nuclear metallicity evolution for a series of disks with varied initial gas fractions (8%, 20%, 40%, and 60%). We merge together these systems on the "e," "f," "h," and "k" orientations. If we initialize the metallicity properties of these disks using the local MZ relation, an assumption that we will relax later in this section, we can track the metallicity evolution and plot the change in the nuclear metallicity, as in Figure 14. This shows that the depressions in the nuclear metallicity that occurred for the low initial gas fractions considered in the previous sections shift toward

less negative, or even positive values, as the initial gas fraction is raised. This transition is caused by the increasing dominance of the enriched metallicity over the dynamical metallicity, primarily owing to the higher star formation rates in the higher gas fraction systems.

These highest gas fraction systems, however, are not natural analogs to galaxies in the local universe. Therefore, our choice to initialize the metallicity properties of these systems using the local MZ relation comes into question. Instead, we should consider an MZ relation better suited for higher redshifts. A full theoretical understanding of the origin of the MZ relation has not yet been obtained, however, cosmological simulations indicate that the shape of the MZ relation is achieved at early times (i.e., $z > 6$) and that galaxies move along this MZ relation toward higher stellar mass, while the amplitude of the MZ relation slowly increases over time (Davé et al. 2007), in broad consistency with observations (Erb et al. 2006a; Maiolino et al. 2008). Without committing ourselves to a single choice for the high-redshift MZ relation, we can reinitialize the metallicity properties of our galaxies using an MZ relation that is offset by a constant fixed value, δ, toward lower metallicities.

Since our simulations have no metallicity dependence, re-normalizing the MZ relation has no effect on the enriched metallicity, but lowers the impact of the dynamical metallicity. The result, shown in the right panel of Figure 14, is that as the MZ relation is shifted to lower metallicities, the change in the nuclear metallicity is expected to become increasingly positive. For all choices for the initial MZ relation, the higher gas fraction systems have a median change in metallicity that is more positive than their low gas fraction counterparts.

Using the local MZ relation (i.e., the black line in Figure 14) for systems with relatively low gas fractions, we find that negative changes to the nuclear metallicity are expected in a merger. This is consistent with the observed lowering of the MZ relation. However, as we move to higher gas fractions, or MZ relations better suited for higher redshifts, we find that increases to the nuclear metallicity are expected. This result is caused by shifting the dominant driver of the nuclear metallicity from
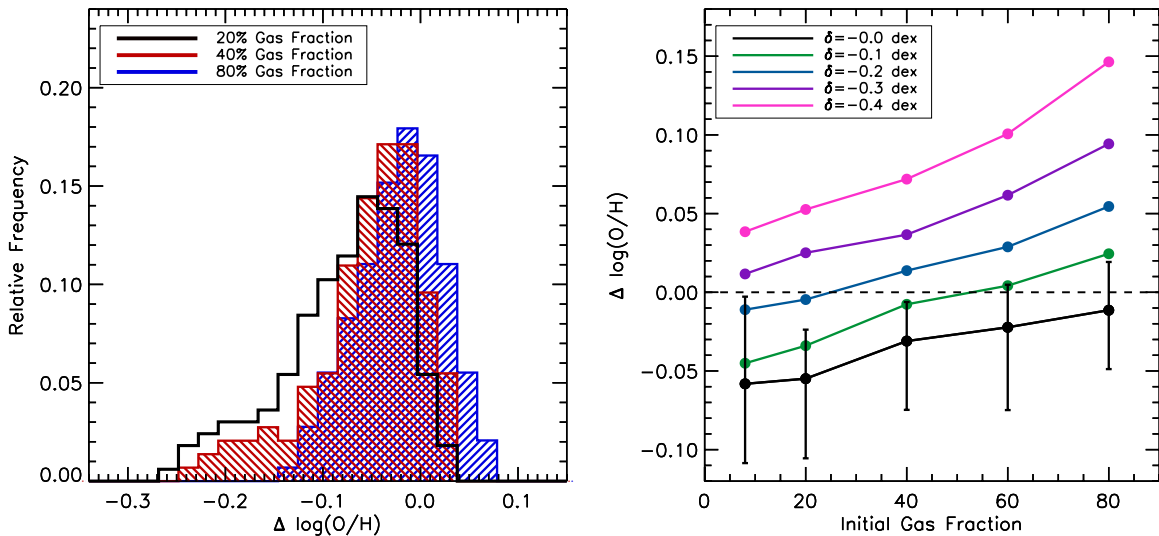
Figure 14. Distribution of changes in the nuclear metallicity for various gas fraction disks (left) and the median change in the nuclear metallicity as a function of gas fraction (right). The offset to the local MZ relation that was used is given by δ in the legend (i.e., $\delta = -0.3$ is consistent with the $z > 2$ MZ relation of Erb et al. 2006a).

(A color version of this figure is available in the online journal.)

metallicity dilution to chemical enrichment. Moreover, if the gas content is sufficiently high, the galactic stellar component cannot efficiently torque down the gas, resulting in moderated early-stage inflows (Hopkins et al. 2009b).

The same merger fundamentals apply to low and high gas fraction disks, independent of their initial metallicities, but the relative increase in the role of chemical enrichment with respect to the dynamical metallicity causes higher redshift or gas fraction systems to increase their nuclear metallicities during the merger process.

Without being overly restrictive about our choice for initial gas fraction or offset from the local MZ relation, high-redshift, gas-rich galaxies are expected to have median increases in their nuclear metallicity when undergoing a merger. Based on this evidence, we predict that the depression that occurs in the MZ relation during galaxy mergers and interactions in the local universe would not occur at higher redshift. Instead, increases in the MZ relation are expected.

5. COMPARISON WITH OBSERVATIONS

Much work in recent years has gone into observationally classifying the metallicity of interacting or close-pair galaxies in the nearby universe (Kewley et al. 2006; Ellison et al. 2008; Peeples et al. 2009; Sol Alonso et al. 2010). In this section, we compare our results directly with these observations. To facilitate this comparison, we parameterize the evolution of the nuclear metallicity in terms of the galactic projected separation. We define the projected separation as $s = r \cos(\xi)$ with ξ being a uniformly distributed random number between 0 and 2π. Since all of our systems are, by definition, interacting systems, this projected separation neglects contributions from truly non-interacting systems. We present the MZ and SZ relations for a simulated population of interacting galaxies.

For these comparisons, we generate a population of progenitor galaxies that contain the metallicity properties of observed field galaxies (Shields 1990; Belley & Roy 1992; Zaritsky et al. 1994; MacArthur et al. 2004). We use a Gaussian distribution for the nuclear metallicity selection with a mean value consistent with the MZ relation of Tremonti et al. (2004) with a

constant standard deviation across mass bins of $\sigma = 0.1$ dex. The metallicity scale length is taken from a Gaussian distribution with a mean gradient consistent with Zaritsky et al. (1994) of $h_z = h/0.2$ with $\sigma = 0.3 h_z$.

The initial metallicity properties of each galaxy in each snapshot are assigned based on the above criteria. Our ability to pick metallicity properties of the progenitor disks in our post-processing analysis is a consequence of not having a dynamical dependence on metals or allowing mixing. This lets us sample the parameter space of initial disk metallicity properties thoroughly, without rerunning simulations.

5.1. The Mass–Metallicity Relation for Interacting Galaxies

The MZ relation for our simulated interacting galaxies is shown in Figure 15. We select galaxies with projected separations less than 30 kpc—the same as was used in Ellison et al. (2008). We plot the MZ relation in Figure 15. The result is a depressed MZ relation with an average depression of 0.07 dex, which is in agreement with the observed depression of 0.05–0.10 dex (Ellison et al. 2008).

Unlike luminosity, which can increase dramatically during merger-induced starburst activity, the stellar mass of an interacting galaxy will change only by a modest factor. Therefore, the evolution of galaxies on the MZ relation is driven by changes to the nuclear metallicity, not stellar mass. In the simulation analysis, we are able to quickly determine a system's stellar mass. The stellar masses for the close-pair systems included in the Ellison et al. (2008) sample have had their stellar masses determined via optical and IR colors (Kauffmann et al. 2003; Tremonti et al. 2004) which have been shown to compare well with the spectrally determined stellar masses (Drory et al. 2004). Assuming that the observationally determined stellar masses are not strongly affected by ongoing starburst activity, the depression in both the observed and simulated MZ relation is being caused entirely by changes to the nuclear metallicity—not by changes in the galactic luminosity or stellar mass.

The depression in our simulated MZ relation would be slightly smaller if we included a set of field galaxies that lie on the MZ relation, but appear close in projected separation (i.e., if we
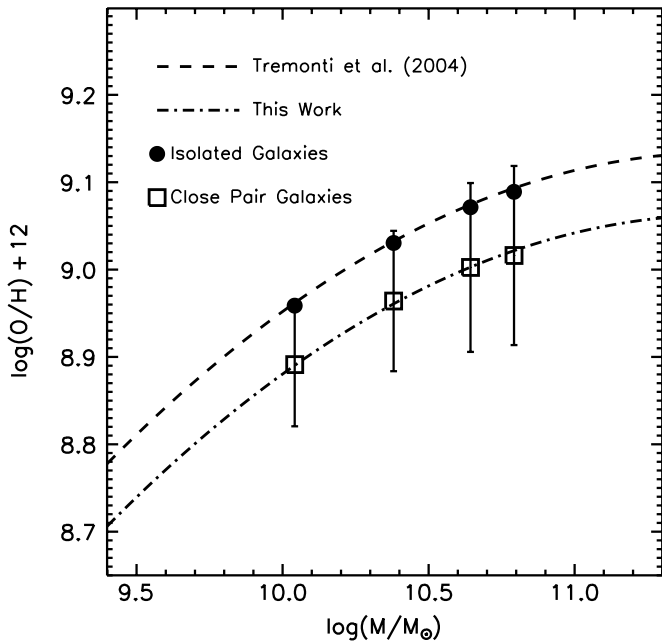
Figure 15. Simulated mass–metallicity relationship for interacting galaxies is shown. The progenitor galaxy MZ relationship from Tremonti et al. (2004) is indicated along with the second-order best fit from our simulation results.

Figure 16. Evolution of two galaxies from one merger simulation is shown. The numbered arrows follow the evolution of the galaxies as they (1) approach first pericenter passage with an unchanging nuclear metallicity, (2) increase their separation while diluting the nuclear metallicity, (3) come together for the second time with notable contributions to the nuclear metallicity from star formation, and (4) lower their nuclear metallicity as they approach final coalescence.

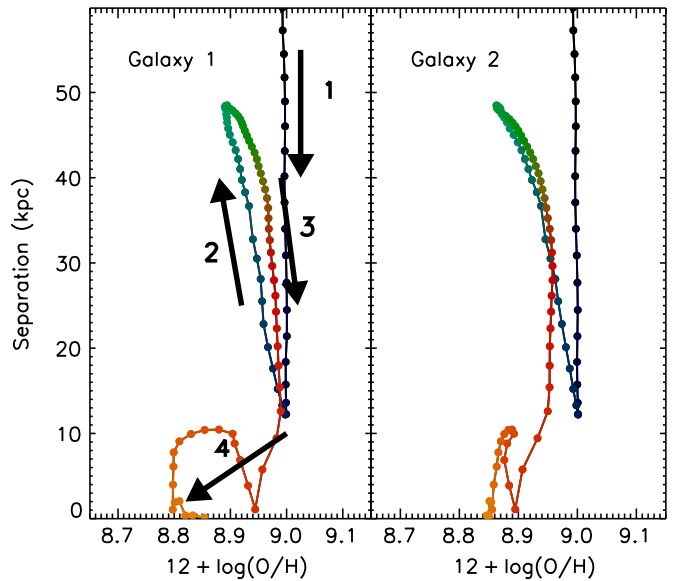(A color version of this figure is available in the online journal.)

included a population of interlopers). This result gives a comprehensive reproduction of the depression in the MZ relation for interacting galaxies that accounts for all relevant physics and the intrinsic scatter in the initial metallicity properties of the progenitor galaxies, while covering a reasonable portion of merger phase space.

5.2. Separation versus Metallicity

Figure 16 shows an example of two galaxies ("C" galaxies) from one merger simulation (the "e" orientation) moving in SZ space as they approach coalescence. The evolution can be broken down into four distinct stages, as marked by arrows in Figure 16. First, the galaxies approach first pericenter passage at relatively constant nuclear metallicities. Second, the galaxies separate as gas inflows dilute their nuclear metallicity. Third, the galaxies begin falling back together, with star formation causing a significant amount of chemical enrichment. And, finally, the galaxies undergo strong gas inflows that further dilute their nuclear metallicities as they approach coalescence.

The details of this SZ evolution will change substantially with the merger orientation. However, we can gather from Figure 11 that all four stages of this evolution will be somewhat generic. Namely, galaxies will present constant nuclear metallicities as they approach each other for the first time and strongly depressed nuclear metallicities as they approach final coalescence, with mildly depressed nuclear metallicities in between.

Using the evolutionary track of Figure 16, we can develop some expectations for the distribution of galaxies in SZ space. Clearly, we expect close-pair galaxies to show depressed nuclear metallicities. In addition, we can expect depressed metallicities out to large galactic separations. While the largest nuclear metallicity depressions are expected around close separations, widely separated interacting galaxies show mildly depressed nuclear metallicities after interacting with their companion. The observability of these trends can be assessed by using our entire merger library and converting real separations into projected separations.

The distribution of all simulated galaxies in SZ space is shown in Figure 17 along with data from Kewley et al. (2006). The distribution of our simulated galaxies, shown with the colored contours in the lower half of Figure 17, coincides with many of the observed systems, which are presented in the histogram in the top half of Figure 17. There is a trend toward lower metallicities with close separations. However, this trend is very mild and the most-extreme low-separation low-metallicity objects from the observed sample are not reproduced by our models. Despite this difference, it should be noted that our simulations agree with the majority of the observed objects from Kewley et al. (2006), and there is a systematic but subtle drop in the simulated nuclear metallicity as the galaxies decrease their projected separation.

We note that the overall distribution of simulated galaxies in SZ space is relatively featureless, as evidenced by the contours in Figure 17. The nuclear metallicity depressions present at both small and large separations in Figure 16 are washed out as a result of projecting the physical separations, the wide variety of metallicity dilution versus separations that result from different spin–orbit couplings, and the scatter in the initial nuclear metallicities as prescribed by the MZ relation. In addition, while late-stage mergers (e.g., stage 4 in Figure 16) present the largest depressions in nuclear metallicity, they only last for a short period of time compared to the overall merger process. Since we place equal weight on every time step for every simulation when determining the distribution of simulated galaxies in Figure 17, the highly depressed late-stage mergers will naturally have a less dramatic impact.

Several factors can influence the distribution of our model galaxies in SZ space. In particular, the (in)completeness of our merger library and the metal enrichment scheme will influence the resulting SZ relation. We discuss both of these factors in the following sub-sections, so that we may better understand the disagreement between our models and the observations at low separations and low metallicities. However, we also note that
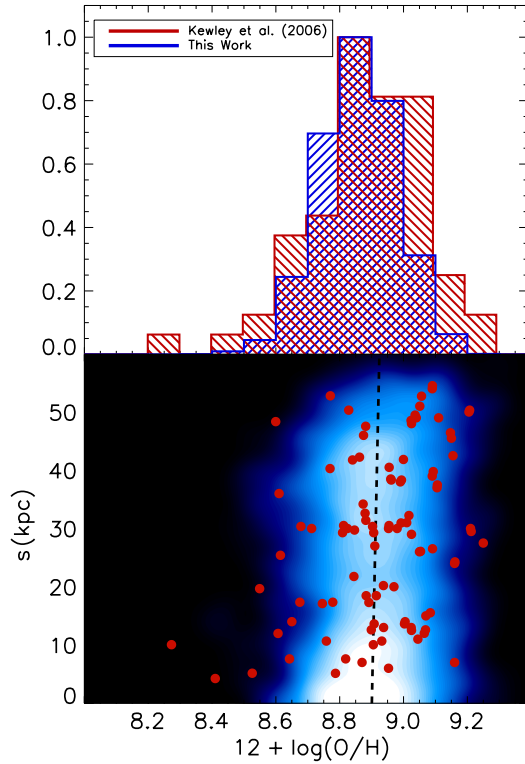
Figure 17. Relative frequency of galaxies in metallicity space (top) and the simulated separation–metallicity relationship along with the data from Kewley et al. (2006) (bottom) are shown. The majority of observed points from Kewley et al. (2006) are coincident with our simulated galaxies, with the exception of the low-metallicity, low-separation tail. Our simulated galaxies show a depression in the nuclear metallicity for close-pair galaxies, however this depression is less dramatic than is required to explain the low-metallicity, low-separation tail observed in Kewley et al. (2006).

(A color version of this figure is available in the online journal.)

additional observations would help clarify how common these low-separation, low-metallicity objects are.

5.2.1. Merger Library Completeness

Although the merger library used in this work was fairly comprehensive, there is a significant portion of merger parameter space that has not been explored. Perhaps this could explain why we do not reproduce the low-separation, low-metallicity objects. We can describe our exploration of merger parameter space with two components: variations of initial isolated galaxies models and merger configuration parameters.

Additional merger configurations (i.e., variations to the orbital orientation and angular momentum) are unlikely to yield surprising results. Out of all of our merger simulations, a maximum depression of about 0.3 dex was found, with many depressions being must less drastic. To achieve the lowest-metallicity objects found in Kewley et al. (2006), depressions of $\sim$0.6–0.7 dex would be required. It seems unlikely that the isolated galaxy models used in this study will reproduce very low metallicity objects, even with a more extensive exploration of merger orientations.

On the other hand, galaxy models that are significantly different from the ones used in this study, such as low-mass galaxies, could fill out a new region in SZ space. For example, galaxies with initial stellar masses of $M_s \sim 10^9 M_\odot$ will have initial nuclear metallicities of $12 + \log(\text{O/H}) \sim 8.6$ and could have their nuclear metallicities depressed to $\sim$8.3 or 8.4 during the merger. More generally, it seems likely that the lowest-

metallicity objects of Kewley et al. (2006) are likely merging systems that had low metallicities prior to the onset of the merger which may be a reasonable possibility given the low B-band luminosities associated with these objects. These systems may be reproduced by our simulations when we include a more extensive set of initial galaxy models.

5.2.2. Approximating Delayed Mixing

Although oxygen abundances are well approximated by an instantaneous enrichment model, this does not necessarily imply that metals produced in supernovae instantaneously migrate to H II regions. Specifically, we can relax our assumption that the metallicity of an SPH particle should be instantaneously identical to the metallicity of an H II region. Our analysis calculated the nuclear metallicity from the current metallicities of gas particles. While the metals produced in core-collapse supernovae are quickly returned to the ISM ($\sim 10^7$ years) and supernovae remnants cool and fade into the ambient ISM over similar timescales ($\sim 10^6$ years), there could then be some additional delay before this gas is sufficiently mixed with the surrounding medium and ends up in H II regions. In particular, we expect the metals produced by supernovae to affect the *next* generation of H II regions. As a first approximation, this does not require a change to our simulations, but rather a change to our post-processing analysis.

We can define an effective H II region metallicity that is given by the metallicity that the SPH particle had one generation of star formation ago. If the number of generations of star formation is given by

$$N_*(t) = \frac{1}{M} \int_0^t \frac{dM_*}{dt'} dt', \qquad (17)$$

where M is the particle mass, then the effective H II region metal content is given by

$$M_Z'(t) = \begin{cases} M_{Z,\text{init}} + yM(N_* - 1) & \text{if } N_* \geqslant 1 \\ M_{Z,\text{init}} & \text{if } N_* < 1 \end{cases}, \qquad (18)$$

which reflects the particle's metallicity one generation of star formation in the past.
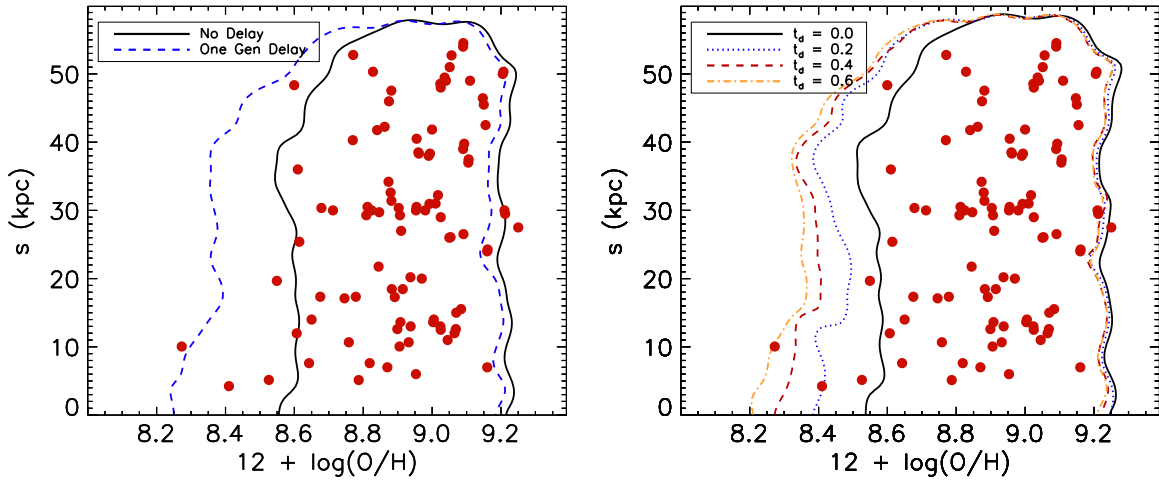
This delayed chemical enrichment scheme gives an SZ relation, shown in the left panel of Figure 18, which has a low-metallicity tail that is qualitatively similar to the observed galaxies. This does not imply that our previous calculation of the nuclear metallicity using the non-delayed chemical enrichment values were incorrect, but rather that the assumption of instantaneous transition of metals into H II regions may be overly restrictive. This is a plausible explanation, provided that the associated delay times are reasonable estimates for the timescale over which supernova ejecta would mix and diffuse into the ISM.

If we parameterize an effective H II region metallicity in terms of a delay time, rather than an integrated star formation rate, we can get an estimate for the required delay time. Rather than neglecting the enrichment from the last generation of star formation, we neglect the enrichment that occurred over the past t_d years. The effective metal content of a particle is then given by

$$M_Z'(t) = \begin{cases} M_{Z,\text{init}} + y \int_0^{t-t_d} \frac{dM_*}{dt'} dt' & \text{if } t \geqslant t_d \\ M_{Z,\text{init}} & \text{if } t < t_d \end{cases}, \qquad (19)$$

where t_d is the assumed time delay.

16

Figure 18. Simulated separation–metallicity relationship is shown using a delayed chemical enrichment scheme. Newly formed metals are allowed to contribute to the H II region metallicity measurements only after the SPH particle in which they reside undergoes an integrated star formation rate equal to its own mass (left) or after a specified delay time, t_d, in Gyr (right). This effectively delays metal enrichment.

(A color version of this figure is available in the online journal.)

This time-delayed chemical enrichment scheme gives an SZ relation, shown in the right panel of Figure 18, where larger delay times lead to systematic decreases in the inferred metallicity of close pairs. This is similar to those seen in the left panel of Figure 18, but with an explicit time dependence. The delay times required for our simulations to match observations is of the order of a few 10^8 years, which is comparable to estimates for the metal mixing timescale of newly produced metals into the ISM (Oey 2003; Scalo & Elmegreen 2004). We conclude that delaying the transfer of metals from supernova remnants to H II regions is important to consider; however, it is unclear whether these long mixing times are appropriate for the extreme environments in merging galaxy nuclei where external forces, gas inflows, high gas densities, and large star formation rates are present.

6. DISCUSSION

6.1. Predictions for Galaxies with High Gas Content

The results of Section 4.4 demonstrate that merger-induced metallicity evolution is heavily dependent upon gas content, specifically, higher gas fraction disks produce less nuclear metallicity depression than lower gas fraction disks (see, e.g., Figure 14). In the extreme, high gas content mergers may even yield significant *enhancements* of central metallicity, a result that emerges both because of the increased impact of enrichment from star formation as well as because nuclear gas inflows are suppressed when the gas fraction is very high (Hopkins et al. 2009b).

As a consequence of these trends, we expect that the nuclear metallicities of gas-rich merging galaxies will be similar to, or greater than, an appropriately matched quiescent sample. This is in contrast to the depression of nuclear metallicity observed in low gas content mergers which was the focus of this paper. Such considerations may be applicable at high redshift where current observations suggest that galaxies contain significantly higher gas fractions (Tacconi et al. 2010; Erb et al. 2006b) and suppressed metallicity at fixed galaxy mass (Erb et al. 2006a; Maiolino et al. 2008) or for less-massive gas-rich galaxies in the local universe (Catinella et al. 2010).

The predicted metallicity enhancements in gas-rich merging systems were also noted in a recent paper by Perez et al. (2011) using similar methods. While both works observed similar metallicity enhancements, the timing was not identical and purported cause of these effects were very different. The Perez et al. (2011) model shows rapid metallicity enhancement during early stages of the merger primarily as a result of rapid star formation owing to disk instabilities in the gas-rich system (see, e.g., their Figures 8 and 9). Such effects occur prior to, or during the early stages of, the merger and are therefore decoupled from the final coalescence stage. In our model, the gas-rich disks are designed to be stable a priori, and therefore the metallicity enhancements are driven by intense star formation triggered by the merger. While the end result is the same, namely metallicity enhancements, the relative timing and strength of the vigorous star formation, the metallicity dilution owing to inflows, and the metallicity enhancement owing to star formation are fundamentally different, and therefore potentially discernible via observations.

We caution, however, that the galaxy merger simulations carried out here may require some generalization before they are directly applicable at high redshifts. Effects such as the higher UV background, higher merger rate, and direct fueling of low-metallicity gas via the surrounding intergalactic medium at high redshifts may be of significant influence in the observed metallicity of galaxies. And numerical uncertainties, such as the proper treatment of feedback from star formation and accreting black holes, will invariably need to be explored.

6.2. Future Considerations: An Improved Chemical Enrichment Model

By comparing our models of interacting galaxies to the observed MZ and SZ relations we have refined our understanding of the factors at play during the metallicity evolution of galaxies. It is crucial to point out (yet rarely done so), however, that numerical results such as ours are based upon the ability to robustly track a number of complicated and interrelated astrophysical processes. While we consider our sub-resolution models to be well motivated and well tested, we admit that there are straightforward improvements to these models which will allow

for more stringent tests of our physical picture. We now take a moment to outline these future improvements to our models.

The chemical enrichment model employed here tracks a global metallicity through a single scalar variable that is continuously updated assuming that the entire solar yield (assumed to be a mass fraction of 0.02) is instantaneously recycled within a single star-forming fluid element (i.e., an SPH particle). We admittedly note the simplicity of this model, but consider the ease with which it is implemented, the straightforward analysis it allows, and its inherent self-consistency as distinct advantages of this approach. The instantaneous recycling approximation is also justified because we compare to oxygen derived metallicities, and oxygen is thought to be recycled on a short ($\sim 10^7$ years) timescale through core-collapse supernovae. Moreover, in a practical sense, similar models have been employed in nearly every SPH code over the last two decades which makes our results easy to gauge within the existing theoretical framework.

There are, however, avenues in which distinct progress can be made to our chemical enrichment model. Efforts toward this end have been pioneered by a number of authors over the last $\sim$5–10 years (see, e.g., Kawata 2001; Tornatore et al. 2007; Scannapieco et al. 2005; Oppenheimer & Davé 2008; Kim et al. 2009, to name a few) by employing two common features: metallicity-dependent cooling and more complex enrichment schemes that explicitly track various species and their time-dependent release. Our gas recycling scheme is particularly well suited for including mass return by a single stellar population. As individual star particles are converted back to interstellar gas, they can straightforwardly carry with them the appropriate enrichment from Type I and II supernovae as well as mass loss from massive young stars and AGB stars. Such an approach is necessary to study trends in abundance ratios, such as those observed in the centers of elliptical galaxies.

Additional accuracy may also be gained by including sub-resolution models for the turbulent diffusion of metals (see, e.g., Wadsley et al. 2008; Shen et al. 2010). Coupled to an advanced enrichment algorithm, a physically motivated procedure for diffusing metals will allow enrichment to occur locally but still have global influences if conditions warrant. Such methods have been shown to be important for tracking metallicity in cosmological simulations (e.g., Shen et al. 2010) and we intend to assess their influence in isolated and merging galactic systems.

Finally, the comparisons between the models and the observations can be significantly improved by actually tracking the detailed line emission using three-dimensional radiative transfer (Jonsson et al. 2010). As efforts to produce data cubes with full spatial and spectral information are developed (e.g., Rich et al. 2010), full metallicity maps can be produced and directly compared to our simulations. Radiative transfer in our simulations will shed light on any additional information that may be encoded in the line profiles and allow for a more even-handed comparison.

7. CONCLUSION

Using numerical simulations, we have investigated the impact that mergers have on galactic nuclear metallicity. Our models include the capability of describing star formation, chemical enrichment, gas recycling, and star-formation-driven winds. The analysis performed here relies upon the ability to accurately track the spatial and temporal return of metals to the

ISM enabled by our stochastic gas-recycling algorithm within GADGET (see Section 2.2).

One of the primary results of this work is to reinforce the notion that galaxy mergers, and their attending gravitational tidal forces, generate significant inflows of gas shown explicitly in Figures 11 and 12 (see also Rupke et al. 2010a; Montuori et al. 2010; Perez et al. 2011). These inflows transport metal-poor gas into the nuclear region and reinforce the generic connection between close galaxy interactions and nuclear metallicity dilution—no matter how many close passages occur.

Merger-induced gaseous inflows are, however, not the only factor influencing the nuclear metallicity, and this paper quantifies the competing effects of enrichment from star formation (Section 4.1.1), gas consumption (Section 4.1.2), and galactic winds (Section 4.1.3). Our models provide a physical template to understand nuclear metallicity evolution and lead us to conclude that merger-induced metallicity dilution and chemical enrichment from star formation drive the nuclear metallicity, while gas consumption and galactic winds play a secondary role to modulate the efficiency of the primary processes.

We have made a distinct effort in this work to directly compare our models to observations, allowing us to validate the physical evolutionary model that we have presented and associate observable trends with the various stages of the merger evolution. We find that the merger-induced depressions of nuclear metallicity are typically $\sim$0.07 dex, an offset similar to that observed to the MZ relation for close pairs in SDSS (Ellison et al. 2008). The models also demonstrate that central depressions of metallicity are time dependent owing to the specific merger orbit, the galaxies' spin–orbit coupling, and varying structural properties of the galaxies. When compared to the observed SZ relation of Kewley et al. (2006), the models generally show a similar trend to produce lower central metallicities at smaller separations. The precise role of interactions is difficult to discern, however, because of the significant scatter in the relations (see Equation (17) and the discussion in Section 5.2). Future comparisons in which galaxies are morphologically classified according to merger stage or separated according to IR luminosity or star formation rate may be better suited to isolate the true effects of the interaction.

This work also demonstrates that the progenitor gas content can have a profound influence on the resulting merger-induced metallicity dilution. Mergers between gas-rich progenitors can yield systematic metallicity enhancement, as opposed to metallicity dilution (see Section 4.4 and specifically Figure 14). In our picture, central metallicity enrichment comes from vigorous merger-induced star formation that can compensate for and eventually overcome the merger-induced inflow of metal-poor gas. This view is slightly different than put forth in recent work by Perez et al. (2011), which argues that disk instabilities and clump formation drive rapid star formation and subsequent metal enrichment. But once these processes occur, which is typically early in the merger process, the story becomes similar to when the galaxies have low gas content. By studying the detailed correlations between merger stage, pair separation, central metallicity, and metallicity gradients, in both observations and the models, future work will allow for a better understanding of the (merger and enrichment) processes at work.

REFERENCES

Barnes, J. E., & Hernquist, L. 1996, ApJ, 471, 115
Barnes, J. E., & Hernquist, L. E. 1991, ApJ, 370, L65

Belley, J., & Roy, J. 1992, ApJS, 78, 61
Catinella, B., Schiminovich, D., Kauffmann, G., et al. 2010, MNRAS, 403, 683
Cox, T. J., Dutta, S. N., Di Matteo, T., et al. 2006a, ApJ, 650, 791
Cox, T. J., Jonsson, P., Primack, J. R., & Somerville, R. S. 2006b, MNRAS, 373, 1013
Davé, R., Finlator, K., & Oppenheimer, B. D. 2007, EAS Pub. Ser., 24, 183
Di Matteo, T., Springel, V., & Hernquist, L. 2005, Nature, 433, 604
D'Onghia, E., Vogelsberger, M., Faucher-Giguere, C., & Hernquist, L. 2010, ApJ, 725, 353
Drory, N., Bender, R., & Hopp, U. 2004, ApJ, 616, L103
Ekta, B., & Chengalur, J. N. 2010, MNRAS, 406, 1238
Ellison, S. L., Patton, D. R., Simard, L., & McConnachie, A. W. 2008, AJ, 135, 1877
Erb, D. K., Shapley, A. E., Pettini, M., et al. 2006a, ApJ, 644, 813
Erb, D. K., Steidel, C. C., Shapley, A. E., et al. 2006b, ApJ, 646, 107
Hernquist, L. 1990, ApJ, 356, 359
Hopkins, P. F., Cox, T. J., Dutta, S. N., et al. 2009a, ApJS, 181, 135
Hopkins, P. F., Cox, T. J., Younger, J. D., & Hernquist, L. 2009b, ApJ, 691, 1168
Hopkins, P. F., & Hernquist, L. 2006, ApJS, 166, 1
Hopkins, P. F., Hernquist, L., Cox, T. J., Dutta, S. N., & Rothberg, B. 2008, ApJ, 679, 156
Hopkins, P. F., Hernquist, L., Cox, T. J., Robertson, B., & Krause, E. 2007, ApJ, 669, 45
Hopkins, P. F., Lauer, T. R., Cox, T. J., Hernquist, L., & Kormendy, J. 2009c, ApJS, 181, 486
Iono, D., Yun, M. S., & Mihos, J. C. 2004, ApJ, 616, 199
Jonsson, P., Groves, B., & Cox, T. J. 2010, MNRAS, 403, 17
Jungwiert, B., Combes, F., & Palouš, J. 2001, A&A, 376, 85
Katz, N., Weinberg, D. H., & Hernquist, L. 1996, ApJS, 105, 19
Kauffmann, G., Heckman, T. M., White, S. D. M., et al. 2003, MNRAS, 341, 33
Kawata, D. 2001, ApJ, 558, 598
Kawata, D., & Gibson, B. K. 2003, MNRAS, 340, 908
Kennicutt, R. C., Jr. 1998, ApJ, 498, 541
Kewley, L. J., Geller, M. J., & Barton, E. J. 2006, AJ, 131, 2004
Kewley, L. J., Rupke, D., Jabran Zahid, H., Geller, M. J., & Barton, E. J. 2010, ApJ, 721, L48
Kim, J., Wise, J. H., & Abel, T. 2009, ApJ, 694, L123
Leitherer, C., Ortiz Otálvaro, P. A., Bresolin, F., et al. 2010, ApJS, 189, 309
Leitherer, C., Schaerer, D., Goldader, J. D., et al. 1999, ApJS, 123, 3
Leitner, S. N., & Kravtsov, A. V. 2011, ApJ, 734, 48
Lequeux, J., Peimbert, M., Rayo, J. F., Serrano, A., & Torres-Peimbert, S. 1979, A&A, 80, 155
Lia, C., Portinari, L., & Carraro, G. 2002, MNRAS, 330, 821
MacArthur, L. A., Courteau, S., Bell, E., & Holtzman, J. A. 2004, ApJS, 152, 175
Maiolino, R., Nagao, T., Grazian, A., et al. 2008, A&A, 488, 463
Martínez-Serrano, F. J., Serna, A., Domínguez-Tenreiro, R., & Mollá, M. 2008, MNRAS, 388, 39
McKee, C. F., & Ostriker, J. P. 1977, ApJ, 218, 148

Michel-Dansac, L., Lambas, D. G., Alonso, M. S., & Tissera, P. 2008, MNRAS, 386, L82
Mihos, J. C., & Hernquist, L. 1994a, ApJ, 437, L47
Mihos, J. C., & Hernquist, L. 1994b, ApJ, 431, L9
Mihos, J. C., & Hernquist, L. 1996, ApJ, 464, 641
Mo, H. J., Mao, S., & White, S. D. M. 1998, MNRAS, 295, 319
Montuori, M., Di Matteo, P., Lehnert, M. D., Combes, F., & Semelin, B. 2010, A&A, 518, A56
Oey, M. S. 2003, in IAU Symp. 212, A Massive Star Odyssey: From Main Sequence to Supernova, ed. K. van der Hucht, A. Herrero, & C. Esteban (Cambridge: Cambridge Univ. Press), 620
Okamoto, T., Eke, V. R., Frenk, C. S., & Jenkins, A. 2005, MNRAS, 363, 1299
Oppenheimer, B. D., & Davé, R. 2008, MNRAS, 387, 577
Peeples, M. S., Pogge, R. W., & Stanek, K. Z. 2009, ApJ, 695, 259
Perez, J., Michel-Dansac, L., & Tissera, P. 2011, MNRAS, 417, 580
Perez, M. J., Tissera, P. B., Scannapieco, C., Lambas, D. G., & de Rossi, M. E. 2006, A&A, 459, 361
Rich, J. A., Dopita, M. A., Kewley, L. J., & Rupke, D. S. N. 2010, ApJ, 721, 505
Robertson, B., Bullock, J. S., Cox, T. J., et al. 2006a, ApJ, 645, 986
Robertson, B., Cox, T. J., Hernquist, L., et al. 2006b, ApJ, 641, 21
Robertson, B., Hernquist, L., Cox, T. J., et al. 2006c, ApJ, 641, 90
Rubin, V. C., Ford, W. K., Jr., & Whitmore, B. C. 1984, ApJ, 281, L21
Rupke, D. S., Veilleux, S., & Sanders, D. B. 2005, ApJS, 160, 115
Rupke, D. S. N., Kewley, L. J., & Barnes, J. E. 2010a, ApJ, 710, L156
Rupke, D. S. N., Kewley, L. J., & Chien, L. 2010b, ApJ, 723, 1255
Rupke, D. S. N., Veilleux, S., & Baker, A. J. 2008, ApJ, 674, 172
Scalo, J., & Elmegreen, B. G. 2004, ARA&A, 42, 275
Scannapieco, C., Tissera, P. B., White, S. D. M., & Springel, V. 2005, MNRAS, 364, 552
Schmidt, M. 1959, ApJ, 129, 243
Shen, S., Wadsley, J., & Stinson, G. 2010, MNRAS, 407, 1581
Shields, G. A. 1990, ARA&A, 28, 525
Sol Alonso, M., Michel-Dansac, L., & Lambas, D. G. 2010, A&A, 514, A57
Springel, V. 2005, MNRAS, 364, 1105
Springel, V., Di Matteo, T., & Hernquist, L. 2005, MNRAS, 361, 776
Springel, V., & Hernquist, L. 2002, MNRAS, 333, 649
Springel, V., & Hernquist, L. 2003, MNRAS, 339, 289
Springel, V., & White, S. D. M. 1999, MNRAS, 307, 162
Steinmetz, M., & Mueller, E. 1994, A&A, 281, L97
Stinson, G., Seth, A., Katz, N., et al. 2006, MNRAS, 373, 1074
Tacconi, L. J., Genzel, R., Neri, R., et al. 2010, Nature, 463, 781
Toomre, A., & Toomre, J. 1972, ApJ, 178, 623
Tornatore, L., Borgani, S., Dolag, K., & Matteucci, F. 2007, MNRAS, 382, 1050
Tremonti, C. A., Heckman, T. M., Kauffmann, G., et al. 2004, ApJ, 613, 898
Vázquez, G. A., & Leitherer, C. 2005, ApJ, 621, 695
Veilleux, S., Cecil, G., & Bland-Hawthorn, J. 2005, ARA&A, 43, 769
Wadsley, J. W., Veeravalli, G., & Couchman, H. M. P. 2008, MNRAS, 387, 427
Wiersma, R. P. C., Schaye, J., Theuns, T., Dalla Vecchia, C., & Tornatore, L. 2009, MNRAS, 399, 574
Zaritsky, D., Kennicutt, R. C., Jr., & Huchra, J. P. 1994, ApJ, 420, 87